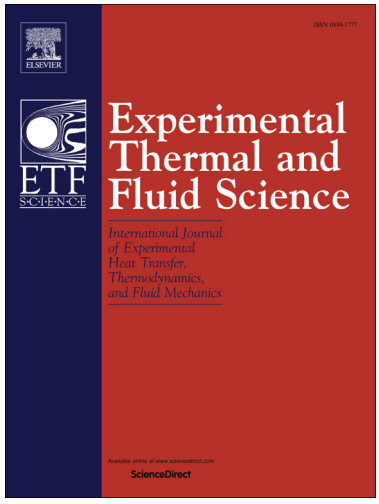

Interfacial friction in upward annular gas–liquid two-phase flow in pipes

Aliyu Musa Aliyu, Yahaya Danjuma Baba, Liyun Lao, Hoi Yeung, Kyung Chun Kim

PII: S0894-1777(17)30035-3
DOI: http://dx.doi.org/10.1016/j.expthermflusci.2017.02.006
Reference: ETF 9008

To appear in: *Experimental Thermal and Fluid Science*

Received Date: 18 June 2016
Revised Date: 1 February 2017
Accepted Date: 4 February 2017

Please cite this article as: A.M. Aliyu, Y.D. Baba, L. Lao, H. Yeung, K.C. Kim, Interfacial friction in upward annular gas–liquid two-phase flow in pipes, *Experimental Thermal and Fluid Science* (2017), doi: http://dx.doi.org/10.1016/j.expthermflusci.2017.02.006

Experimental Thermal and Fluid Science, Vol. 84, June 2017, pp. 90-109
DOI:10.1016/j.expthermflusci.2017.02.006

Interfacial friction in upward annular gas–liquid two-phase flow in pipes

Aliyu Musa Aliyu[1], Yahaya Danjuma Baba[2], Liyun Lao[3], Hoi Yeung[3], Kyung Chun Kim[1*]

[1]School of Mechanical Engineering, Pusan National University, 609-735, Busan, Republic of Korea
[2]Department of Chemical and Petroleum Engineering, Afe Babalola University, PMB 5454, Nigeria
[3]Oil and Gas Engineering Centre, Cranfield University, Bedfordshire MK43 0AL, United Kingdom

Abstract

Accurate prediction of interfacial friction between the gas and liquid in annular two-phase flow in pipes is essential for the proper modelling of pressure drop and heat transfer coefficient in pipeline systems. Many empirical relationships have been obtained over the last half century. However, they are restricted to limited superficial liquid and gas velocity ranges, essentially apply to atmospheric pressures, and the relationships are only relevant for pipes with inner diameters between 10 and 50 mm. In this study, we carried out experiments in a large diameter flow loop of 101.6 mm internal diameter with the superficial gas and liquid ranges of 11–29 m/s and 0.1–1.0 m/s respectively. An examination of published interfacial friction factor correlations was carried out using a diverse database which was collected from the open literature for vertical annular flow. The database includes measurements in pipes of 16–127 mm inner diameter for the liquid film thickness, interfacial shear stress, and pressure gradient for air-water, air-water/glycerol, and argon-water flows. Eleven studies are represented with experimental pressures of up to 6 bar. Significant discrepancies were found between many of the published correlations and the large pipe data, primarily in the thick film region at low interfacial shear stress. A correlation for the interfacial friction factor was hence derived using the extensive database. The correlation includes dimensionless numbers for the effect of the diameter across pipe scales to be better represented and better fit the wide range of experimental conditions, fluid properties, and operating pressures.

Keywords: Co-current annular flow, pressure gradient, interfacial shear stress, liquid film thickness, vertical two-phase flow.

*Corresponding author
E-mail address: kckim@pusan.ac.kr (K.C. Kim)

Nomenclature

A. Roman

A	[m^2]	Cross-sectional area
D	[m]	Pipe internal diameter
e	[-]	Entrained liquid fraction
Fr	[-]	Froude number = $u/\sqrt{gD}$
f	[-]	Interfacial friction factor
g	[m/s^2]	Acceleration due to gravity
L	[m]	Pipe length
$\dot{m}$	[kg/s]	Phase mass flow rate
P	[Pa]	Local pressure
ΔP	[Pa]	Differential pressure
$-\frac{dP}{dz}$	[Pa/m]	Pressure gradient
Re	[-]	Reynolds number = $\rho u D/\mu$
t	[m]	Film thickness
u	[m/s]	Phase superficial velocity
x	[-]	Gas quality = $\rho_g u_{sg}/(\rho_g u_{sg} + \rho_l u_{sl})$
z	[m]	Axial distance along pipe

B. Greek

δ	Unit depends on quantity in question	Error in quantity indicated in bracket
ε	[-]	Void fraction
γ	[-]	Liquid droplet holdup
ν	m^2/s	Kinematic viscosity
μ	[kg/s-m]	Dynamic viscosity
ρ	[kg/m^3]	Density
σ	[N/m]	Surface tension
τ	[Pa]	Shear stress

C. Subscripts

c	Core
d	Droplet
e	Entrainment
g	Gas phase
i	Interfacial
l	Liquid phase
lf	Liquid film
s	Single phase
sg	Superficial gas
sl	Superficial liquid
w	Wall

1 Introduction

1.1 Background

Gas–liquid annular two-phase flow frequently occurs in many practical industrial applications. Common examples are gas condensates in oil and gas pipelines, evaporating and condensing flows in refrigeration systems and heat exchangers, and steam–water flows during nuclear reactor core cooling. This flow regime is characterised by the flow of liquid at the pipe inner wall periphery with a gas core flowing in the central region. At the interface between the two fluids, ripples and/or disturbance waves can be observed, the latter with high crests that can be sheared off at high gas velocities, which leads to liquid droplets being entrained in a highly turbulent gas core. These droplets can be re-deposited on the liquid film.

Because of the interactions of mass, momentum, and occasionally heat transfer at the interface, annular two-phase flows are complex and do not readily lend themselves to analytical modelling. Therefore, physically based models such as those based on two- or three-field models are usually solved numerically to obtain estimations of the phase fractions or pressure drop, which requires closure laws. Relations for closure laws include the fraction of liquid entrained as droplets and the interfacial friction factor, and they heavily rely on relevant experimental data.

The closure for interfacial friction factor deserves particular attention, because drag on the gas–liquid interface is dominant in the force balance (Belt et al. [1]). As will be shown later, the interfacial friction factor is an essential parameter in the force balance that couples the wavy film and the turbulent gas core. It is important to note that the interfacial friction factor differs from the two-phase friction factor. For the latter, a homogenous mixture is assumed to flow in the pipe and may be flow regime independent; therefore, mixture properties – density, viscosity and velocity – are hence defined and used. On the other hand, properties of the flowing gas are used in the case of the interfacial friction factor, where a momentum balance is done with the liquid film (not pipe wall) as boundary. Correlations for the interfacial friction factor derived by earlier investigators go back to Wallis [2] who used the analogy of single phase flow to propose a linear approximation to the

53 turbulent flow relationship in rough pipes. This works only for a small range of film thicknesses in the
54 low interfacial shear stress region. Since then, modifications based on his theory have been made (see
55 Belt et al. [1], [3]–[6]) but these correlations also fit limited ranges of data. Moreover, these do not
56 usually give good estimations when the inner pipe inner diameter goes beyond 100 mm (the observed
57 boundary between small and large diameter pipes).

58 Therefore many authors (Oliemans et al. [7]–Smith et al. [15]) insist that there is a need to
59 increase the knowledge of multiphase flow behaviour for large diameter pipe systems. For instance,
60 Oliemans et al. [7] compared entrainment correlations with large diameter test data and concluded
61 there is not much confidence in the predicted values of the correlations. Kataoka & Ishii [8] showed
62 that the use of the conventional drift flux model for pool void fraction prediction to relatively large
63 pipes was only limited to low gas fluxes, and thus had to develop a new correlation for large systems
64 where annular flow, for example, occurs at higher gas velocities. Disturbance waves which greatly
65 contribute to wall shear stress and are a source of entrained droplets were observed by Azzopardi et al.
66 [16] to be what they called “incoherent” in large diameter pipes. Careful observations revealed that in
67 large pipes, the waves were not perpendicular to the flow direction but were curved “bow waves” and
68 was also observed by Van der Meulen [17]. This contrasts to what obtains in smaller tubes where the
69 waves are continuous around the circumference (see Nedderman and Shearer [18], and Zhao et al.
70 [19]). The study by Omebere-Iyari and Azzopardi [20] on disturbance wave velocity provided strong
71 quantitative indication of pipe diameter effect on the gas–liquid interface behaviour. They established
72 that Pearce’s coefficient, which is proportional the to wave velocity, increases with pipe diameter
73 until it reaches a constant value of 0.9 for large pipe diameters.

74 The foregoing means that the interaction between the fluids is different between the two pipe
75 scales and published data on large diameter pipes is scarce. It is therefore important to focus on
76 understanding the underlying mechanisms and finding more relationships that can apply to large pipes
77 for more optimal designs of pipeline systems.

1.2 Previous interfacial friction factor correlations

Table 1 summarises several previous correlations for the interfacial friction factor in upward gas–liquid annular flow. It is pointed out that the interfacial friction factor is different from the two-phase friction factor which is based on the wall shear stress rather than the interfacial shear stress. The latter considers the flowing fluids as a homogenous mixture such that a mixture density and mixture velocity are used to calculate the wall shear stress and hence frictional pressure drop. Therefore, the prediction methodology is different from what is presented in this paper and correlations for the two-phase friction factor (e.g. Klausner et al. [21], and Cioncolini et al. [22]) are not included in the table. One of the earliest and most widely used correlations for the interfacial friction factor in two-phase flow modelling is that by Wallis [2], which is essentially a linear fit of the friction factor against the non-dimensional film thickness. Many modifications have been made to Wallis' correlation through simple adjustments of the coefficients in order to fit experimental data (Belt et al. [1], Moeck [3], Fore et al. [6], and Fukano and Furukawa [23]).

Table 1: Reported interfacial friction factor correlations used for comparison with the current experimental data

Various correction methods were applied in order to update Wallis' correlation such as raising the dimensionless film thickness to a power (Moeck [3]), introducing a function of the gas Reynolds number (Fore et al. [6]), or introducing a ratio to account for the influence of a change in fluid viscosity (Fukano and Furukawa [23]). As will be shown later, a plot of the Wallis-type correlations against the present data and reported data shows that one curve cannot be used to represent all of these data, as agreements that occur between some data and correlations do not occur with others.

1.3 Experimental data from the open literature

A total of 332 data points were collected for the vertical annular two-phase pressure drop in smooth pipes. The data were obtained from 12 sources using pipes with internal diameters ranging from 5 to 127 mm, including the current data. Key information about the sources in the database is given in Table 2 with a breakdown of selected parameters provided in the histograms in Figure 1. All the data are for macroscale gas–liquid flows obtained with transparent test sections, which allow for visual identification of the flow regime. All data are in the annular flow regimes, so it is assumed that there is little or no contamination from intermittent flow regimes such as slug or churn flows.

Table 2: Experimental data for upward interfacial friction factor (all air/water except stated otherwise)

Development lengths (L/D ratios) for the different datasets as reported by their authors were examined and these are presented in Table 2. This is also shown in the histogram in Figure 1 (b), for which most of the data were collected between 41 and 100 pipe diameters with the largest being that of Owen [32] at 600 pipe diameters with 97 data points. Omebere-Iyari et al. [10] examined vertical two-phase flow with different fluid combinations and concluded that L/D = 40 is sufficient for reasonably well-developed flow after showing that the probability distribution functions (PDFs) of the void fraction have very similar shapes at this value and higher. Their experiments were carried out at 46 bar pressure, and this may have facilitated the relatively short development length of 40 pipe diameters. For the current study, the development length as given in Table 2 is 46 pipe diameters, slightly higher than that of Omebere-Iyari et al. [10]. As will be shown later (in Section 3.2), we observed that at L/D = 46 reasonably developed flow was produced. The inlet condition for the upward section of the serpent pipe may have greatly assisted the relatively short development length. This is because the momentum generated from the preceding downward flowing section is inherited and this aids the upward flow development.

Figure 1: Histograms showing selected parameters of the experimental database given in Table 2

Four sets of data were obtained from experiments large diameter pipes. These sets include the current study (101.6 mm) and those by Van der Meulen [17], Zangana [30], and Skopich [31] who investigated flow in pipes with internal diameters of 127, 127, and 101.6 mm, respectively. The remaining eight data sources are for smaller diameter pipes (less than 100 mm) ranging from 5 to 50.8 mm.

A majority of the measurements in the database are for air–water fluid combinations, except for those of Alia et al. [34], and Fore and Dukler [35], who reported work on fluid combinations of argon–water, and air/glycerine mixtures respectively. For system pressures, these runs range from just below atmospheric pressure (0.9 bar) in the air and water study by Skopich et al. [31] to 6 bar by Alia et al. [34] for argon and water. As shown in Figure 1 (c), the majority lie around atmospheric pressure. Many data points (108) fall between 2 bar (Owen [32]) and 3 bar (Van der Meulen [17]).

The database contains experimental measurements on pressure gradients, and several of the studies include direct measurements for liquid film thickness using conductance probes (the current study, Belt et al. [1], Alia et al. [34], and Wongwises and Kongkiatwanitch [29]). Others determine the liquid film thickness by measuring the cross-sectional void fraction and assuming a geometrically uniform film along the pipe circumference [11], [17], [30], [31]. Owen [32] measured the entrained droplet fraction in the gas core using the method of the isokinetic probe and estimated the droplet flow rate. Others such as Fore et al. [6] measured the entrained fraction by sucking out the film using a porous wall feature and subtracting from the liquid input. The entrained fraction is important in the calculation of interfacial fraction factor from the measured pressure gradient, because the entrained droplets change the properties of the gas core such as its density, and velocity. Belt et al [1] and Fore and Dukler [36] noted that the entrained droplets can in some cases contribute up to 20% of the total pressure gradient. Therefore, where entrainment occurs, this must be accounted for in the momentum balance equation.

We performed experiments in a large diameter flow loop in order to collect data on interfacial friction factor in upwards annular flow. Together with the diverse experimental database collected from the open literature, we will show that earlier correlations for the interfacial friction factor from small pipe measurements do not adequately represent data for large pipes and for conditions when the liquid film is relatively thick. Consequently, a correlation will be proposed that better fits our data as well as those from the diverse sources that cover a wider range of fluid velocities and pipe diameters.

2 Experimental setup and data processing

2.1 Description of flow loop

The experimental setup shown in Figure 2 is the Serpent Rig, an air/water facility at the Oil and Gas Engineering Laboratory of Cranfield University. It is divided into three main parts: the Fluid Supply (air and water) and Metering Area, the Test Area, and the Separation Section. The flow rig receives measured flow rates of water and air from the Flow Metering area to the test rig and finally into the ventilation tank, where the air and water are separated. The water is then returned to the storage tank while the air is vented.

The Test Area consists of the flow loop, which is a pipeline that is approximately 20 m long with an internal diameter of 101.6 mm (4 in.). The loop includes four vertical sections made from ABS (acrylonitrile butadiene styrene) plastic with upward and downward flows and connected by three Perspex 180-degree bends. The two 6-m vertical pipes in the middle are equipped with various instruments that collect all the data. While the right arm of the U is the downward flowing section, the left vertical section is the upward flowing section which is the area of interest of this study and where all the data were collected.

Figure 2: Serpent Rig facility indicating the upward section used for this study

Flow metering equipment includes two air flow meters capable of measuring 0–4250 Sm^3/h of air and a water flow meter with a range of 0.06–16 L/s. Six GE Sensing UNIK 5000 pressure

transducers (0–1.5 barg ±0.04%) are located at positions P2, P5, and P6 for the upward flow section. Conductance probes are installed in the flow rig to measure the liquid film thickness, and a 32×32 grid capacitance wire mesh sensor (WMS) measures the cross-sectionally averaged gas void fraction, which was used to identify the flow regime. Their locations are shown by dotted lines in Figure 2. A DeltaV system and LabVIEW software were used for data acquisition. The DeltaV system records and controls the air flow rates with a fixed sampling rate of 1 Hz, while LabVIEW acquires and records the pressures, film thicknesses, and fluid temperatures using a sampling rate of 100 Hz. Details about the design, calibration, and uncertainty analysis of the instrumentation are given in previous studies [37]–[40].

2.2 Instrumentation

2.2.1 Film thickness probes

The conductance probe is one of the most common techniques for determining liquid holdup in gas – liquid systems. It relies on measurements of electrical impedance between two electrodes in contact with a conducting fluid and several configurations have been over the years depending on the application and channel geometry. Its relative simplicity in application when compared to other methods has been identified as a major advantage as well as the low cost of equipment involved. Further details on types, principle of operation, design, and electronics can be found in the many published articles are available in the open literature (e.g. Coney [41], Koskie et al. [42], Tsocharitzidis et al. [43], and [44]). The film thickness probes used in this study were manufactured in-house and the design is shown schematically in Figure 3.

Figure 3: (a) film thickness sensor spool with four flush-mounted probes (b) details of individual sensor design (all dimensions in mm) (c)) blocks of different diameters used for probe calibration (d) sample of film thickness calibration curve (e) Repeatability tests for film thickness probes showing the mean film thickness at u_{sl} = 0.1 m/s. For more conditions, see Almabrok [37]

The spool consists of four film conductivity sensors which are evenly distributed circumferentially to measure the circumferential distribution of the liquid film thickness at the location where the spool is installed. As shown in Figure 3 (b) the sensing part of the conductivity film thickness probe comprises a 10 mm diameter stainless steel rod and a stainless steel sleeve (18 mm outer diameter by 2 mm wall) arranged concentrically. Between them is a 2 mm thick insulation layer. The end of the sensor is flush with the inner surface of the spool. Each conductor is electrically in contact with the liquid film when the liquid film flows over them, so a conductive bridge is formed. The conductivity and hence voltage between the two conductors is expected to change with the thickness of the water film. The normalised output, i.e. ratio of output voltage to full scale voltage, was used for calibration and measurements, as it minimises measurement errors caused by inconsistent liquid conductivity and environmental factors such as temperature. The calibration was carried out by using acrylic blocks (which like air, are electrical insulators) of known diameters inserted into the probe spool concentrically to form a liquid layer with known thickness. Calibration curves are plotted for the measured film thickness against normalised voltage output obtained offline. Equations of these curves were used to convert online voltages obtained during experiments to film thicknesses. Temperature correction coefficients for the sensors are regularly identified and applied for correcting the temperature drift errors in the film thickness measurement. This is in done in addition to the use of normalised film sensor outputs. The correction is applied to a temperature range of 10–35 °C, which covers the two-phase mixture temperature range 15–22 °C in which the tests were performed. During a test both the water and water/air mixture temperatures were logged so temperature compensation was able to be implemented in order to obtain film thickness values during the offline data processing. The repeatability of the liquid film thickness probes were checked by performing triplicate runs at a constant superficial liquid velocity and the full range of superficial gas velocities between 12.5 and 28.9 m/s. Figure 3 shows a plot of such a test at 0.1 m/s. A standard deviation of 0.1 mm in repeated film thickness measurements was established as a result, and this gives a ±3.3% full scale error in the film thickness measurement. It is also possible that inlet/outlet stability could also add to small changes in the repeatability of the test, and this may have also

contributed in the ±3.3% difference between respective measurements. It was considered that the uncertainty caused by calibration to be much smaller in comparison, and hence negligible, since the calibration curves of the probes give R-square values of 0.99 and above for fifth-degree polynomials.

2.2.2 Wire mesh sensor (WMS)

The capacitance Wire Mesh Sensor (WMS) used for the cross-sectional void distribution measurement at the stated locations along the pipe axis has a 32×32 wire grid (Figure 2 (c)). The sensor, associated electronics and data processing software were provided by Helmholtz–Zentrum Dresden–Rossendorf, Germany. The method of phase fraction distribution measurement in air/water flows using similar WMS has been validated by a number of studies (Prasser et al. [45] and Da Silva et al. [46]). In the sensor assembly, wire electrodes perpendicular to each other are across the flow cross-sectional area.

Figure 4: Capacitance wire mesh sensor used in this study

One set of the perpendicular wires acts as signal sender, while the other acts as receiver. The WMS measures the local permittivity of the fluid in the gaps of each crossing point by continuously applying an excitation voltage (of 5 MHz) to each sender electrode while keeping others at ground potential then synchronously measuring the alternating current flow to all receivers. Based on these measurements, the cross-sectional fluid distribution across the pipe the sensor can be estimated. For the sensor used in this study, the separation between the sender and receiver planes of wires is 2.5 mm. The spacing between two wires in parallel is 3.2 mm. A sampling rate of 1000 frames per second is used for the measurement. Validation studies were carried out on the measurement accuracy of the present WMS system and it was reported by Almabrok et al. [39] that errors of around ±10% are obtainable. Further reading on the theory and principles of operation of the WMS can be found in the works of Prasser et al. [45], Da Silva et al. [47], and Da Silva et al. [48].

2.3 Data processing

2.3.1 Film velocity and entrained droplet fraction

The entrained droplet fraction was calculated from measurements obtained for the liquid film thickness discussed earlier, and the liquid film velocity measurements. Mean liquid film velocity measurements were made using the electrolyte injection method. The method involves injecting sodium chloride electrolyte into the liquid film to create a surge in conductivity. The transit time of a conductivity surge between two identical sensors 100 mm apart in a probe spool is determined using a cross-correlation algorithm in MATLAB. The film velocity is then calculated by dividing the distance by the signal transit time or time delay between the two sensors. The assumption here is that as the liquid films are very thin ($\sim 1-1.5\,mm$), the velocity profile within the film is such that the wave (or structure) velocities are close to the bulk film velocity, meaning velocities with higher uncertainty for the thicker films. Nevertheless, uncertainties of around ±8% in the film velocity measurements were produced and this has been discussed extensively [40].

Using the definitions given in

Figure 5, the measured velocities can then be used to calculate the entrained droplet fraction using the relationship:

$$e = \frac{\dot{m}_l - \dot{m}_{lf}}{\dot{m}_l} = \frac{\rho_l u_{sl} A - \rho_l u_{lf} A_{lf}}{\rho_l u_{sl} A} = 1 - \frac{4 u_{lf} t}{u_{sl} D} \quad (1)$$

where $\dot{m}_l$, and $\dot{m}_{lf}$ are the total liquid flow rate and liquid film flow rate in kg/s, while e, t, u_{lf}, u_{sl}, and D are the entrained liquid fraction, measured film thickness, measured film velocity, liquid superficial velocity and pipe internal diameter respectively. Tabulated and graphical results obtained using Equation (1) for different flow conditions are given in Almabrok [37] and Aliyu et al. [40].

Figure 5: Representation of annular flow with droplets

Figure 6 (a) and (b) show typical examples of time series data collected for the liquid film thickness and pressure gradient. The measurement conditions include a superficial liquid velocity of 1.0 m/s and superficial gas velocity of 18.56 m/s. Data were recorded for 2 minutes per run, but the figures show the behaviour for 10 seconds only. The wavy nature of the liquid film recorded by the conductance probe is clearly seen in Figure 6 (a) with wave heights that are one to two times greater than the thickness of the base film. This behaviour has widely been reported for annular films (Hall Taylor et al. [49], and Sawant et al. [50]).

Figure 6: Examples of time series data for (a) liquid film thickness and (b) pressure gradient with a superficial liquid velocity of 1.0 m/s and superficial gas velocity of 18.56 m/s

For subsequent steady-state analyses, the time series data were averaged over the whole two-minute recording time, as shown in Table 3. For all superficial liquid velocities, the liquid film thickness increases with superficial liquid velocity but decreases with increasing gas velocity. This decrease with gas velocity is asymptotic for vertical upflow regardless of liquid velocity and viscosity (see Fukano and Furukawa [23]). Equation (2) is the steady-state momentum balance for the two-phase mixture flowing upwards in the pipe:

$$-\frac{dP}{dz} = \{\rho_c \varepsilon + \rho_l(1-\varepsilon)\}g + \frac{4}{D}\tau \tag{2}$$

Where ρ_g and ρ_l are the gas and liquid densities respectively; ε is the time-averaged cross-sectional void fraction. The first term on the right hand side of the equation refers to the gravitational component of the pressure gradient; the second is the frictional component with τ being the shear stress, which consists of the wall and interfacial shear stresses:

$$\tau = \frac{1}{2}\left\{f_w \rho_l (1-\varepsilon) u_{lf}^2 + f_i \rho_c \varepsilon (u_c - u_{lf})\left|u_c - u_{lf}\right|\right\} \tag{3}$$

where f_w and f_i are the wall and interfacial friction factors respectively. As shown in Table 3, for all superficial liquid velocities, the liquid pressure gradient increases with the gas superficial velocity. This is easily explained by Equations (2) and (3), where the frictional component of the pressure gradient increases as the superficial fluid velocities increase. Wall friction increases as liquid velocity increases; while interfacial friction increases with increasing slip at the gas–liquid interface, and this is more affected by the core velocity since the liquid velocity does not change by as much.

Table 3: Averaged measured quantities for the air–water system in the upward section of the Serpent Rig

A flow regime map for upward flow was produced using visual observations and this is presented in Figure 7 (a). Flow regimes that are either bubbly or churn are marked as "other" and these have been excluded from the data in Table 3. The regimes were identified with the help of videos made from WMS reconstructed images. Specially designed software was used to stack the images acquired at 1000 fps and these can be played back at slower speeds than real-time. Example snapshots of the videos at u_{sl} = 0.2 m/s are shown in Figure 7 (a) and they were used to differentiate flow at u_{sl} = 9.7, and 12.09 m/s. It can be seen that for the former condition, the gas core is not continuous. Large liquid lumps can be seen to be torn off from base film. Such a flow was not classified as annular since some up and down oscillatory movement was observed. The regime was ultimately classified as "churn" flow and screened out from those used for the subsequent analyses in this paper. At critical conditions near flow regime transition regions, identification is difficult to achieve with the naked eye, and this underscores the importance of using the WMS. Conversely, the snapshot on the top right-hand corner of Figure 7 (a) was classified as annular where a distinct gas–liquid interface and a continuous gas phase can be seen.

Figure 7 (b) is a plot of measured pressure gradient (dP/dz) for the upward flow section. For all superficial liquid velocities, dP/dz values decrease with increasing gas velocity. There is a decrease

in dP/dz because increasing gas void fraction results in decreasing cross-sectional liquid holdup and the liquid contribution to the gravitational pressure gradient also decreases. However, a minimum is reached when increasing the gas velocity results in the frictional component of dP/dz equalling the gravitational component. This results in a competition between inertia and gravity forces and oscillatory behaviour is observed with the liquid. The minimum dP/dz is a critical point corresponding to a flow regime transition from churn to annular flow (see Hewitt and Hall-Taylor [51], McQuillan and Whalley [52], and Hewitt [53]). Further increasing the gas velocity causes the pressure gradient to increase due to the increasing dominance of the frictional component over the gravitational component. The flow is now in the annular region and the conditions for this study were chosen from this region indicated by the closed markers in Figure 7 (b).This is agrees with our visual observations as well as the reconstructed WMS images.

Figure 7: Effect of fluid superficial velocities on flow regime map produced by visual observations aided by WMS visualisation

2.3.2 Determination of interfacial friction factor from measurements

From the foregoing discussion, the pressure gradient, liquid film thickness and velocity measurements obtained for this study were verified to be in the annular region. These were used to calculate the interfacial friction factor, which in fully developed annular two-phase flow is defined as:

$$f_i = \frac{2\tau_i}{\rho_g u_{sg}^2} \tag{4}$$

The superficial gas velocity u_{sg} in this work is calculated based on the whole pipe cross-sectional area. In many cases, droplets are torn off from the crests of the liquid film (or atomised) and become entrained in the gas core, thereby affecting its density. The interfacial friction factor thus becomes:

$$f_i = \frac{2\tau_i}{\rho_c u_c^2} \tag{5}$$

where the subscript *c* denotes the core region. The following three steps are used to determine the core velocity, core density, and the interfacial friction factor respectively:

1. Core velocity

Estimation of the core density ρ_c requires knowledge of the liquid film velocity, which was determined experimentally for the present dataset. Details are well documented for the measurement technique using cross correlation of conductance signals from adjacent axial probes and the corresponding uncertainties [37], [38], [40], [54]. The core velocity u_c is estimated by writing a mass balance of the gas input, which yields the relationship for the mean velocity for the gas core (see Vieira et al. [55]):

$$u_c = \frac{(u_{sg} + u_{sl}e)D^2}{(D-2t)^2} \tag{6}$$

where t is the measured mean liquid film thickness assuming it is circumferentially uniform, and e is the entrained droplet fraction determined experimentally. In cases where experimental data for e was not available, it was calculated using the correlation of Cioncolini and Thome [56]. Other empirical correlations exist such as those of Ishii and Mishima [57], and Sawant et al. [58].

Figure 8: Representation and notation of the various phases (film, gas, and droplets) occupying the total pipe area. Subscript *d* denotes droplets. Where γ, ε, and ε_c are the droplet holdup, void fraction and core void fraction respectively (Cioncolini et al. [22]**)**

2. Core density

The density ρ_c of a gas core laden with entrained droplets used in Equation (5) is calculated as the arithmetic mean of the pure gas and liquid droplet densities:

$$\rho_c = (1-\varepsilon_c)\rho_l + \varepsilon_c\rho_g \tag{7}$$

where ε_c (Figure 8) is the gas core void fraction estimated as:

$$\varepsilon_c = \frac{\varepsilon}{\varepsilon + \gamma(1-\varepsilon)} \tag{8}$$

ε is the cross-sectionally averaged void fraction, and γ is the droplet holdup. An expression for the droplet holdup γ can be obtained using the definition of the entrained droplet fraction e which is the ratio of the entrained liquid droplet mass flow rate $\dot{m}_d$ to that of the total liquid mass flow rate $\dot{m}_l$ i.e.:

$$e = \frac{\dot{m}_d}{\dot{m}_l} = \frac{\rho_l u_d A_d}{\rho_l u_{sl} A} = \frac{u_d A_d}{u_{sl} A} \tag{9}$$

If the phase slip between the droplets and the carrier gas is ignored, the droplets travel at the velocity of the carrier gas, therefore $u_d = u_g$. Equation (9) now becomes:

$$e = \frac{u_g A_d}{u_{sl} A} = \frac{\frac{u_{sg}}{\varepsilon} A_d}{u_{sl} A} \tag{10}$$

Substituting the relation for the cross-sectional area occupied by the droplets A_d based on the phase splits as shown in Figure 8, we can rewrite Equation (10) as follows:

$$e = \frac{u_{sg}}{u_{sl}} \frac{\gamma(1-\varepsilon)}{\varepsilon} \tag{11}$$

The gas quality x is defined as the ratio of the gas mass flux to the total gas mass flux; i.e. $x = \rho_g u_{sg} / (\rho_g u_{sg} + \rho_l u_{sl})$. Rearranging it as $\frac{u_{sg}}{u_{sl}} = \frac{x\rho_l}{(1-x)\rho_g}$ and substituting in Equation (11) yields:

$$e = \frac{x\rho_l}{(1-x)\rho_g} \frac{\gamma(1-\varepsilon)}{\varepsilon} \tag{12}$$

which can be rearranged to the following to give an expression for the droplet holdup for use in Equation (8):

$$\gamma = e \frac{\varepsilon}{1-\varepsilon} \frac{1-x}{x} \frac{\rho_g}{\rho_l} \tag{13}$$

3. Interfacial shear stress

The interfacial shear stress τ_i is obtained from a momentum balance around the gas core in the axial direction of the flow, as shown in Figure 9. It is assumed that the flow is fully developed, at steady state, and at equilibrium where the rate of droplet entrainment equals the rate of droplet deposition. Therefore,

$$\tau_i = \frac{D - 2t}{4}\left(-\frac{dP}{dz} - \rho_c g\right) \tag{14}$$

where $-dP/dz$ is the measured pressure gradient. For a detailed derivation of Equation (14), see Fore et al. [6], and Wongwises and Kongkiatwanitch [29]. Equations (6)–(14) can then be used to calculate the interfacial friction factor as defined in Equation (5).

Figure 9: Control volume for the momentum balance in Equation (14). Based on the schematic by Wongwises and Kongkiatwanitch [29]

3 Discussion of results

3.1 Flow regime maps

The conditions for the current experiments and those obtained from the literature were plotted together on the Taitel et al [59] flow regime map, as shown in Figure 10. It can be seen that all the data points chosen for this study fall in the annular flow region. Taitel et al's [59] flow regime map was constructed using physically based mechanisms which underlie each transition. They also derived models for the transitions based on these mechanisms. Along with the Hewitt and Roberts [60] flow regime map (Figure 11Figure 11), it is one of the most widely used for gas–liquid flow in vertical pipes. The test conditions range from the near annular transition (e.g. Van der Meulen [17], and Alia et al. [34]) to the fully annular flow region (e.g. Shearer and Nedderman [61]). Flow regime transitions are not sharp and occur within a range of superficial fluid velocities, which could be affected by the liquid viscosities and densities of liquid and gas phases. As a result, data points that may seem to fall in the churn flow region of the map were actually observed to be annular flow. For example, Alia et al. [34] report data that are deeply within the annular flow regime region when plotted on the Hewitt and Roberts [60] flow regime map shown in Figure 11Figure 11, but these points fall in the annular flow region nearer the transition areas when plotted on the Taitel et al. [59] flow regime map. However, in the flow regime map published by Shell [62] and shown in Figure 12, the conditions for the entire database can be seen to be in the annular flow region. The flow regime

map is based on the gas and liquid Froude numbers on the horizontal and vertical axes respectively. Here, the Froude numbers are densimetric and defined as follows:

$$Fr_g = u_{sg}\sqrt{\frac{\rho_g}{(\rho_l-\rho_g)gD}}, Fr_l = u_{sl}\sqrt{\frac{\rho_l}{(\rho_l-\rho_g)gD}} \quad (15)$$

Figure 10: Experimental data against the Taitel et al. [59] **flow regime map at (a) 1 bar (b) 2.5 bar pressure**

Figure 11: Experimental data bank against Hewitt and Roberts [60] **flow regime map showing all data are in the annular flow regime**

Figure 12: Experimental databank against the Shell [62] **flow regime mapFilm thickness, void fraction, and flow development**

The measurement station within the dotted circle of the upward flowing section of the flow rig in Figure 2 is located at 46 pipe diameters from the bottom bend. An extensive study on axial variation of measured quantities along the straight sections of the rig was reported in the doctoral thesis of Almabrok [37]. It showed that a significant reduction in entrance effects is already achieved on reaching the top location. Time series and probability distribution functions of film thickness, pressures, and void fraction exhibited similar established flow at the top (L/D = 46 from the U-bend) and middle positions (L/D = 28). These tendencies substantially differ from those observed at the bottom position (L/D = 5) which exhibited flow maldistributions due to bend effects. Confirmation of flow development was done by observing slow-motion videos made by stacking individual WMS frames (achieved using specially designed software).

Figure 13: Normalised liquid film thickness axial development in the upwards flowing section of the rig (See Almabrok [37] **for more)**

Figure 13 shows normalised mean film thicknesses obtained from the conductance probes at the stated axial positions for u_{sl} = 0.2, 0.3, and 0.48 m/s. The normalised film thickness here is defined as the ratio of film thickness at other L/D positions to that at L/D = 46 (i.e. $t_{norm} = t/t_{L/D=46}$). This means that t_{norm} at 46 pipe diameters is unity. The error bars shown in the graphs were calculated as errors propagated from the ±3.3% uncertainty in the film thickness probes; and these are $\sqrt{3.3^2 + 3.3^2}$ = ±4.7%. It can be seen that there is minimal change in the normalised mean film thickness between the middle and bottom positions. Similarly, Figure 14Figure 14 shows the normalised void fraction obtained from the WMS at L/D = 5, 28, and 46 positions from the bottom U-bend for u_{sl} = 0.2, 0.48, and 1.0 m/s. The void fractions were normalised with respect to that at L/D = 46 such that $\varepsilon_{norm} = \varepsilon/\varepsilon_{L/D=46}$ and ε_{norm} = 1 at L/D = 46. The error bars shown in the graphs for ε_{norm} were calculated as errors propagated from the ±10.0% uncertainty in the WMS; and these are $\sqrt{10.0^2 + 10.0^2}$ = ±14.4%. Again, as shown, the ratios at the bottom position reach up to 1.2 in contrast to those obtained at the middle which converges very close to 1. The effect of superficial liquid velocity can be seen from Figure 13 and Figure 14. As liquid velocity increases, there is increasing disparity between the film thickness/void fraction ratios at the bottom positions of the pipe for different gas velocities. However, the ratios become similar by converging towards unity for all conditions once the flow reaches the middle part of the pipe. While L/D = 46 is one of the least in the database collected (see Table 2), flow development is helped by the momentum gathered in the downward flowing section and transferred as the flow negotiates the bend to the upward flowing section. Therefore, the data used for the analyses in this paper are those at L/D = 46, represent highly developed upwards annular flow (fully developed flow is difficult to achieve and requires very long pipes). Additional details can be found in Almabrok [37].

Figure 14: Normalised gas void fraction axial development in the upwards flowing section of the rig

3.2 Comparison of experimental friction factors and existing correlations

The interfacial friction has an inverse relationship with the gas Reynolds number as expected, which is akin to the turbulent flow region of the Moody Chart for single-phase flow. The gas Reynolds number used is here is based on the superficial gas velocity and pipe diameter i.e.

$$Re_g = \frac{\rho_g u_{sg} D}{\mu_g} \tag{16}$$

Fore et al. [6] note that the at sufficiently high Reynolds numbers, the interfacial friction factor reaches an asymptotic value and at such conditions, the friction factor becomes dependent only on the relative liquid film thickness. Nevertheless, it is clear that the gas Reynolds number is a candidate for interfacial friction factor correlation, and one curve that is a function of the Reynolds number only cannot represent all the data. Other parameters representing the different experimental conditions, pipe scales, and fluid properties need to be considered. This is perhaps evident from the different trends exhibited by the various datasets, because the ranges of liquid flow rates and pipe sizes widely differ. Error analysis of the interfacial friction factor is given in the Appendix, and this shows relative errors of ±6–14%.

A plot of f_i vs t/D values for the current experiments, as well as those from previous studies is given in

Figure 15. It can be seen that there are general under- and over-predictions that are magnified as t/D increases. For instance, the measurements by Shearer and Nedderman [33] and those by Owen [32] are within 50% of the values predicted by the correlations of Wallis [2], Moeck [3], and Fore et al. [6] at low t/D values, but they deviate by more than 10 times at higher values. One reason for the general agreement at small t/D values could be that most data and correlations were obtained at conditions in the full annular region, where the films are thinner and smoother. These are far from the

transition region where thick and rough films are found. With the dimensionless film thickness being able to show the behaviour of the interfacial friction factor within the various regions of annular flow, it is therefore a relevant parameter in correlating interfacial friction factor data.

Figure 15: Experimental interfacial friction factors versus superficial gas Reynolds number

Figure 16: Comparison of current and other experimental friction factors with Wallis-type correlations

Another group of f_i correlations have Wallis-type structure but no functional dependence on t/D. Examples are those by Ambrosini et al. [26], and Holt et al. [28] who use several combinations of the bulk gas Reynolds and Weber numbers. Asali et al. [5] and Ambrosini et al. [26] used correlations with the film thickness (t^+) non-dimensionlised by the friction velocity. Implementation of these equations is iterative since they are implicit functions of the interfacial friction factor. As shown in Figure 17 (e) and (h), these correlations provide good predictions in the higher shear regions, where the films are thinner and smoother but rapidly deteriorate for thicker films. Asali et al. [5] and Ambrosini et al. [26] used similar databases for their correlations, which included data obtained from pipes with internal diameter of 10–42 mm and fluid combinations of helium and hydrocarbons/glycerine mixtures, in contrast to the air or steam/water combinations mostly considered in the present database.

Hori et al. [24] opted for a direct power law relationship for the friction factor using the Reynolds and Froude numbers of the gas and liquid. The Froude numbers are defined as follows:

$$Fr_g = \frac{u_{sg}}{\sqrt{gD}}, Fr_l = \frac{u_{sl}}{\sqrt{gD}} \tag{17}$$

Their correlation produced good estimations at low values of the interfacial friction factor. However, as shown in Figure 17 (d), substantial over-estimations occur at high values of f_i corresponding to low

gas flow regions where the liquid films are thick and rough. Again, this is because the experimental conditions do not cover these regions. Wongwises and Kongkiatwanitch [29] also used a power law relationship for their friction factors obtained in a 29-mm pipe at atmospheric pressure. They used the gas Reynolds number and the non-dimensional film thickness t/D as their correlating dimensionless numbers and their correlation was less successful over the experimental database.

In summary, these interfacial friction factor correlations were developed with data obtained for small pressure ranges. For example, Fukano and Furukawa [23] carried out measurements at around 1 bar, Holt et al. [28] used 0.2–1.5 bar, Ambrosini et al. [26] used 0.2–1.9 bar, and Asali et al. [5] used 1–2 bar. Only Fore et al. [6] had a wider range of test pressures than the current database at 3.4–17 bar for experiments with air–water, air–water/glycerine, and nitrogen–water gas–liquid combinations. However, their experiments were conducted with a small diameter pipe and in the thin film region, in contrast to the current database of larger and smaller-diameter pipes containing much thicker liquid films.

It is clear that there is a need to extend the applicable range of prediction methods for the interfacial friction factor. While a mechanistic or physical approach is desirable, it has not been achieved due to the difficulties introduced in annular two-phase flow by high turbulence and complex momentum transfer across the highly deformable gas–liquid interface. Improvements may be achieved using correlations over broader ranges of flow conditions and tube sizes. We therefore propose a new correlation using a more diverse database.

Figure 17: Comparison of 332 interfacial friction factor data points with predictions of various correlations

3.3 Correlation of interfacial friction factor

Fore et al. [6] noted that the Wallis correlation and other correlations with Wallis-type dependency on t/D do not adequately account for changes in Reynolds number in annular flow. They are best applied in annular flow where the dependence on the Reynolds number is minimal, such as for thin, smooth films. In such a situation, the friction factor depends on only the dimensionless film thickness and has been argued to have linear dependence (e.g. Belt et al [1]). However, this conclusion is based on only a small number of data points collected in a small-diameter pipe in the annular flow regime. For films that are deeply in the annular regime and especially in large pipes, the flow behaviour cannot be dictated by the rough film mechanism because these films are smooth and thin.

Azzopardi [37] and Jayanti et al. [64] show that the waves on the crests of the film in large pipes are circumferentially incoherent, meaning that they cover only a part of the tube circumference. They therefore do not solely dictate the flow behaviour, and the flowing gas plays a vital role in determining many of the flow characteristics, including interfacial friction. It is thus necessary to fit the friction factor data in order to reflect other parameters that dictate the flow behaviour, not only the dimensionless film thickness as in the classic correlations. The following form is therefore proposed for the interfacial friction factor:

$$f_i = f_s\left[1 + a(t/D)^b Re_g^j Fr_g^k\right]^l \tag{18}$$

Where $f_s = 0.046 Re_g^{0.2}$. Equation (18) includes the gas Reynolds and Froude numbers (defined in Equation 17) but essentially retains the form of a Wallis-type correlation. This preserves the behaviour of the Wallis correlation, which works quite well at small values of t/D (Figure 16 and Figure 17). The Reynolds number ensures that the correlation captures inertia changes in the gas core. The gas Froude number is included because it is a ratio of inertial forces of pressure-driven gas/liquid flow to the opposing gravitational force, particularly important for high-velocity gas flows in vertical upward annular two-phase flow. The inertial forces dominate gravitation, resulting in $Fr_g > 1$ and this

548 is termed supercritical flow where the tendency of films to flow downwards is overcome by inertia
549 from the gas flow. $Fr_g \approx 1$ is the critical gas Froude number at the flow reversal point. In fact, authors
550 such as Wallis ([2], [65]) and Barbosa et al. [66] have used $Fr_g > 1$ as a criterion for the transition
551 from churn to annular flow and annular flow. If $Fr_g < 1$, annular flow is not considered to have
552 occurred and the flow is still in the churn regime where film oscillations occur due to the two
553 competing forces. Therefore, the inclusion of the gas Froude number is consistent with the
554 phenomenon of annular flow. Partial correlational analysis with other dimensionless numbers such as
555 the core Reynolds, and Weber numbers as well as the liquid Reynolds number showed that these have
556 little effect on the interfacial friction factor.

557 Non-linear least squares regression with the entire experimental database yields the following
558 correlation:

$$f_i = f_s\left[1 + 0.3(t/D)^{0.12} Re_g^{0.54} Fr_g^{-1.20}\right]^{1.5} \tag{19}$$

559 where Re_g and Fr_g are defined in Equations (16) and (17). The correlation is valid for $D^* > 2$, where
560 $D^* = D/\sqrt{\sigma/g(\rho_l - \rho_g)}$ the dimensionless hydraulic diameter as defined by Kataoka and Ishii [8].
561 Pipes with D^* greater than about 37, corresponding to D = 100 mm, are considered to be large
562 diameter. For $D^* < 2$ corresponding to $D < 5$ mm, Equation (19) may not apply due to lack of
563 representative data (for $D < 5$ mm) in the databank. For such pipes capillary forces will be prevalent
564 and non-dimensional quantities such as the Capillary number (Ca) may be used to correlate data.

565 Figure 18 shows that this correlation fits the data better than any of those in Figure 17 (a)–(m). From
566 the figure, it is evident that there is a clear segregation in the magnitudes of the experimental friction
567 factors along pipe scales, with the larger pipes having higher interfacial friction factors. This might
568 seem surprising at first but is entirely logical since larger pipes produce smaller relative slip between
569 the phases compared to small-diameter pipes (i.e., a lesser value of $(u_c - u_{lf})$).

570

Figure 18: Predictions of proposed correlation compared with entire experimental database

For the gas Reynolds number in the proposed correlation, the positive index of 0.55 may seem inappropriate at first, given that there is always an inverse relationship between friction factors and the Reynolds number or fluid velocity. This is also true in the present case, as the superficial gas velocity inherent in Re_g and Fr_g carries a net negative index of –0.66, which is within the range of –0.6 to –0.89 obtained for the index of Re_g by previous authors in their correlations for f_i (Fore et al. [6], Wongwises and Kongkitatwanitch [29], Hori et al. [24], Ambrosini et al. [26], and Holt et al. [28]). Furthermore, t/D in Equation (19) is raised to a power of 0.1 which is a rather small number indicating a lesser than expected dependence of f_i on film thickness. This was explained by Cioncolini and Thome [67] and Narcy [68] to be because the velocity profile in the film is concentrated in the region near the pipe wall. This near wall region is much smaller than the film thickness, hence the small power on t/D.

The computed statistics (MSE, MAE, etc.) show that the proposed correlation predicts the current database quite well. It exhibits the lowest values of mean square error (MSE) (see Table 4). Although other correlations have comparable values (e.g. those of Asali et al. [5], and Hori et al. [24]), their predictions have much higher mean absolute error and lower number of points within the ±50% error band. Over half of the predicted points lie within the ±50% error band for the correlations reported by Asali et al. [5], Fore et al. [6], and Wongiwises and Kongkiatwanitch [29], as shown in the table. However, these values carry a bias based on the large number of data from small pipes, and the data are mostly for relatively thin films, as shown in

Figure 16 and Figure 17. As stated earlier, the shape, size, and localisation of the waves in large pipes have been shown by many authors in the past to differ from smaller pipes and these features affect the manner in which droplet entrainment/deposition and momentum transfer occur. The new correlation can be used as a closure relationship in numerical codes to produce better predictions

of interfacial friction factor, especially in the thick film regions where the gas velocity is low (around 15–20 m/s) and the gas–liquid interface is rougher.

Table 4: Statistical comparison between predictions of proposed and previous correlations

While no correlations are universally acceptable, due to their limited or lack of physical insight, we suggest a more mechanistic approach for future work. This is not easy since the turbulent gas–liquid interface presents unique challenges of momentum transfer by droplet deposition and entrainment. There are currently no mechanistic models for droplet entrainment and deposition, which adds another layer of difficulty for such a methodology. Another approach towards improvement could be correlations fitted with more local measurements of local phenomena rather than with bulk properties of the film and flowing gas. However, this will require the collation of a large pool of more local measurements such as the disturbance wave heights, wave frequencies for the film, and velocity profiles within both phases. Complete sets are currently scarce or remain largely unpublished. The addition of evaporating, boiling, condensing flows, and data from experiments conducted in microgravity will also expand the applicable ranges of new empirical models. Nevertheless, as shown, the current correlations can be used with more confidence, given that they have been developed from a broader range of flow conditions and pipe diameters than what has been reported.

4 Conclusions

In this study experiments were performed using a large diameter flow loop of 101.6 mm internal diameter within the superficial gas and liquid ranges of 11–29 m/s and 0.1–1.0 m/s respectively. Data on pressure gradient, as well as film thickness were collected in the annular flow regime and these were used to calculate the interfacial friction factor. The effectiveness of using existing prediction methods for the interfacial friction factor was then examined in large-pipe annular flow, as well as in small-pipe flow from a variety of sources. These sources include data from a wide spectrum of flow conditions and pipe sizes. For example, the range of pipe diameters is 20–127 mm, and the data are

obtained from experiments performed with air–water, argon–water, and air–glycerol combinations as the test fluids. The interfacial friction factor is one of the important parameters in determining pressure gradient in the annular flow regime. However, our analyses show that many of the previous correlations can be inadequate when used outside certain ranges of experimental conditions, especially for large industrial pipe simulations. Nevertheless, many of these are used as closure laws in commercial thermal-hydraulic codes based on one-dimensional two- or three-fluid models. The results indicate the following:

- Previous correlations for the interfacial friction factor of vertical annular flow are mostly arithmetic modifications of Wallis correlation ($f_i = 0.005[1 + 300t/D]$), where the intercept and/or factor are changed to fit ranges of experimental conditions.
- Wallis-type correlations which are functions of only t/D give some deviations of f_i predictions for thicker liquid films especially in large diameter pipes.
- The proposed correlation ($f_i = f_s\left[1 + 0.3(t/D)^{0.12}Re_g^{0.54}Fr^{-1.20}\right]^{1.5}$) gives better description of the interfacial friction factor in upward annular flow across pipe scales in the database. It maintains the shape and characteristics of the Wallis-type dependency on the dimensionless film thickness at low t/D values. However, introducing simple functions of the core Reynolds and Froude numbers ensures its relevance for thicker films.

As mentioned, mechanistic methodologies are required to provide more generally applicable models. More studies are needed for optimal design and operation of pipeline systems and other equipment in novel applications such as microchannels for cooling in microelectronics, as well as many traditional cases in oil and gas, refrigeration, heat exchange, and other process industries.

Acknowledgement

A. M. Aliyu and Y. D. Baba would like to express their sincere gratitude to the Nigerian Government for funding their PhDs through the Petroleum Technology Development Fund's Overseas Scholarship Scheme (PTDF/E/OSS/PHD/AMA/622/12 and PTDF/E/OSS/PHD/BYD/532/12). This work was also

supported by the National Research Foundation of Korea (NRF) grant funded by the Korean government (MSIP) through GCRC-SOP (No. 2011-0030013). We also acknowledge the funding provided by the BK21 Plus Program of the School of Mechanical Engineering, Pusan National University, Republic of Korea. For data processing, image reconstruction software, and technical support, we thank Prof. Hampel and his group at Helmholtz-Zentrum Dresden-Rossendorf, Germany, as well as Prof. Da Silva and his group at Universidade Tecnológica Federal do Paraná, Brazil. Finally, we would like to thank the esteemed anonymous referees for their thorough review of this article.

Appendix A

Error estimation for the current friction factor calculations

Error analysis of the calculated variables is important to provide an estimation of uncertainty propagation due to measurements. Here, the quantity of interest is the interfacial friction factor. To estimate it, we substitute Equation (14) in Equation (5), which yields a relationship for calculating the interfacial friction factor in terms of all the measured experimental quantities of the pressure gradient, liquid film thickness, and core density (a function of the measured liquid film velocity):

$$f_i = \frac{\frac{D-2t}{4}\left(-\frac{dP}{dz}-\rho_c g\right)}{\frac{1}{2}\rho_c u_c^2} \tag{A1}$$

The quantities in Equation (A1) that are dominant in the uncertainty determination are $-\frac{dP}{dz}$, ρ_c, t, u_c, and u_{lf}. The uncertainty in f_i is caused by the random errors in the measurements and can be given as a relative error. Thus,

$$\frac{\delta f_i}{f_i} = \sqrt{\frac{(\delta S)^2 + (\delta\rho_c)^2}{(S+\rho_c g)^2} + \left(\frac{\delta t}{D-2t}\right)^2 + \left(\frac{\delta\rho_c}{\rho_c}\right)^2 + \left(\frac{2\delta u_c}{u_c^2}\right)^2} \tag{A2}$$

where $S = -\frac{dP}{dz}$, and δ represents the uncertainties in the respective quantities. For pressure gradient measurements, the uncertainty in $-\frac{dP}{dz}$ is $\pm(\sqrt{(0.04)^2 + (0.04)^2}) = \pm 0.057\%$ based on the manufacturer quoted error of ±0.04% for each transducer. These give 0.42–1.58 Pa/m uncertainty in pressure gradient for the current experiments (See Table 3 for the actual values of pressure gradient

obtained). The specified range of measurement of the transducers is (0–1.5 barg ±0.04%). For film thickness (measurements were between 0.7–1.3 mm), the uncertainty is ±3.3% as estimated by three repeated film measurements; while for the film velocity, it is δu_{lf} = ±8% of local measurements (see Aliyu et al. [40]). The uncertainty in the gas core density is not readily available since they are derived quantities. Therefore, the uncertainties in ρ_c and u_c are deduced from their definitions in Equations (6) and (7), respectively

The uncertainty in ρ_c in Equation (A2) is deduced from the definition of ρ_c in Equation (7). The wetted area A_{lf} of liquid film and the input liquid mass flow rate in Equations (8) and (13) are substituted in Equation (7) and simplified. This yields an expression for ρ_c in terms of u_{lf}:

$$\rho_c = \rho_l - \frac{\varepsilon(\rho_l - \rho_g)}{\varepsilon + (1 - \frac{\rho_l u_{lf} A_{lf}}{\dot{m}_l})\frac{\varepsilon}{(1-\varepsilon)}\frac{1-x}{x}\frac{\rho_g}{\rho_l}} \tag{A3}$$

where $\dot{m}_l$ is the liquid input mass flow rate (in kg/s). Now,

$$\delta(\rho_c) = \delta(u_{lf})\frac{\partial \rho_c}{\partial u_{lf}} \tag{A4}$$

where $\frac{\partial \rho_c}{\partial u_{lf}}$ is obtained by differentiating Equation (A3). After rearranging,

$$\frac{\partial \rho_c}{\partial u_{lf}} = \frac{\varepsilon(\rho_l - \rho_g)\frac{\varepsilon}{1-\varepsilon}\frac{1-x}{x}\frac{\rho_g}{\rho_l}\frac{\rho_l A_{lf}}{\dot{m}_l}}{\left[\varepsilon + \left(1 - \frac{\rho_l A_{lf}}{\dot{m}_l}\right)\frac{\varepsilon}{1-\varepsilon}\frac{1-x}{x}\frac{\rho_g}{\rho_l}\right]^2} \tag{A5}$$

For the uncertainty in the core flow velocity u_c, its definition in Equation (6) is used to deduce $\delta(u_c)$:

$$\delta(u_c) = \sqrt{\left[\delta(e)\frac{\partial u_c}{\partial e}\right]^2 + \left[\delta(t)\frac{\partial u_c}{\partial t}\right]^2} \tag{A6}$$

where $\frac{\partial u_c}{\partial e}$ and $\frac{\partial u_c}{\partial t}$ are obtained by differentiating Equation (6) with respect to e and t respectively. Thus,

$$\frac{\partial u_c}{\partial e} = \frac{u_{sl}}{(D-2t)^2} \tag{A7}$$

and

$$\frac{\partial u_c}{\partial t} = \frac{4t(u_{sg} + u_{sl}e)}{(D-2t)^3} \tag{A8}$$

where the entrained droplet fraction e is determined experimentally from the measured liquid film velocity using Equation (1). Lastly, the percentage error in f_i for each experimental condition is calculated as follows:

$$Err(f_i) = \frac{\delta f_i}{f_i} \times 100\% \quad \text{(A9)}$$

As similarly shown in our previous publication [40], the errors for determining the interfacial friction factor from the experimental measurements using Equations (A1)–(A9) are between 5 and 15%, with a majority of errors in the vicinity of 7–13% (Figure A 1).

Figure A 1: Experimental uncertainties in f_i

References

[1] R. J. Belt, J. M. C. Van't Westende, and L. M. Portela, "Prediction of the interfacial shear-stress in vertical annular flow," *Int. J. Multiph. Flow*, vol. 35, no. 7, pp. 689–697, 2009.

[2] G. B. Wallis, *One Dimensional Two-Phase Flow*, vol. null. New York: McGraw-Hill, 1969.

[3] E. O. Moeck, "Annular-dispersed two-phase flow and critical heat flux," p. 206, 1970.

[4] W. H. Henstock and T. J. Hanratty, "The interfacial drag and the height of the wall layer in annular flows," *AIChE J.*, vol. 22, no. 6, pp. 990–1000, 1976.

[5] J. C. Asali, T. J. Hanratty, and P. Andreussi, "Interfacial Drag and Film Height for Vertical Annular Flow," *Am. Inst. Chem. Eng.*, vol. 31, no. 6, pp. 895–902, 1985.

[6] L. . Fore, S. . Beus, and R. . Bauer, "Interfacial friction in gas–liquid annular flow: analogies to full and transition roughness," *Int. J. Multiph. Flow*, vol. 26, no. 11, pp. 1755–1769, Nov. 2000.

[7] R. V. A. Oliemans, B. F. M. F. M. Pots, and N. Trompé, "Modelling of annular dispersed two-phase flow in vertical pipes," *Int. J. Multiph. Flow*, vol. 12, no. 5, pp. 711–732, Sep. 1986.

[8] I. Kataoka and M. Ishii, "Drift flux model for large diameter pipe and new correlation for pool void fraction," *Int. J. Heat Mass Transf.*, vol. 30, no. 9, pp. 1927–1939, Sep. 1987.

[9] N. K. Omebere-Iyari, "The effect of pipe diameter and pressure in vertical two-phase flow,"

University of Nottingham, 2006.

[10] N. K. Omebere-iyari, B. J. Azzopardi, D. Lucas, M. Beyer, and H. Prasser, "The characteristics of gas / liquid flow in large risers at high pressures," vol. 34, pp. 461–476, 2008.

[11] R. Kaji and B. J. Azzopardi, "The effect of pipe diameter on the structure of gas / liquid flow in vertical pipes," *Int. J. Multiph. Flow*, vol. 36, no. 4, pp. 303–313, 2010.

[12] D. J. Peng, M. Ahmad, C. P. Hale, O. K. Matar, and G. F. Hewitt, "Flow regime transitions in large diameter pipes," in *7th International Conference on Multiphase Flow*, 2010, pp. 1–9.

[13] L. Lao, L. Xing, and H. Yeung, "Behaviours of elongated bubbles in a large diameter riser," no. 1998, pp. 381–392, 2012.

[14] J. P. Schlegel, S. Miwa, S. Chen, T. Hibiki, and M. Ishii, "Experimental study of two-phase flow structure in large diameter pipes," *Exp. Therm. Fluid Sci.*, vol. 41, no. 2012, pp. 12–22, Sep. 2012.

[15] T. R. Smith, J. P. Schlegel, T. Hibiki, and M. Ishii, "Two-phase flow structure in large diameter pipes," *Int. J. Heat Fluid Flow*, vol. 33, no. 1, pp. 156–167, Feb. 2012.

[16] B. J. Azzopardi, S. Taylor, and D. B. Gibbons, "Annular two phase flow in a large diameter tube," Harwell, Oxfordshire, UK, 1982.

[17] G. P. Van der Meulen, "Churn-Annular Gas-Liquid Flows in Large Diameter Vertical Pipes," University of Nottingham, 2012.

[18] R. M. Nedderman and C. J. Shearer, "The motion and frequency of large disturbance waves in annular two-phase flow of air-water mixtures," *Chem. Eng. Sci.*, vol. 18, no. 10, pp. 661–670, Oct. 1963.

[19] Y. Zhao, C. N. Markides, O. K. Matar, and G. F. Hewitt, "Disturbance wave development in two-phase gas-liquid upwards vertical annular flow," *Int. J. Multiph. Flow*, vol. 55, pp. 111–129, 2013.

[20] N. K. Omebere-Iyari and B. J. Azzopardi, "A Study of Flow Patterns for Gas/Liquid Flow in Small Diameter Tubes," *Chem. Eng. Res. Des.*, vol. 85, no. 2, pp. 180–192, 2007.

[21] J. F. Klausner, B. T. Chao, and S. L. Soo, "An Improved Correlation for Two-Phase Frictional Pressure Drop in Boiling and Adiabatic Downflow in the Annular Flow Regime," *Proc. Inst. Mech. Eng. Part C J. Mech. Eng. Sci.*, vol. 205, no. 5, pp. 317–328, Sep. 1991.

[22] A. Cioncolini, J. R. Thome, and C. Lombardi, “Unified macro-to-microscale method to predict two-phase frictional pressure drops of annular flows,” *Int. J. Multiph. Flow*, vol. 35, no. 12, pp. 1138–1148, 2009.

[23] T. Fukano and T. Furukawa, “Prediction of the effects of liquid viscosity on interfacial shear stress and frictional pressure drop in vertical upward gas–liquid annular flow,” *Int. J. Multiph. Flow*, vol. 24, no. 4, pp. 587–603, Jun. 1998.

[24] K. Hori, M. Nakasamomi, K. Nishikawa, and K. Sekoguchi, “Study of ripple region in annular two-phase flow (Third report, effect of liquid viscosity on gas-liquid interfacial character and friction factor),” *Trans. Jap. Soc. Mech. Eng.*, vol. 44, no. 387, pp. 3847–3856, 1978.

[25] T. Fukano, A. Ito, K. Miyabe, and Y. Takamatsu, “Liquid films flowing concurrently with air in horizontal duct. (6th report Generation of disturbance waves and its relation with the breakdown of liquid film),” *Transactions of the Japan Society of Mechanical Engineers Series B*, vol. 51, no. 462. pp. 503–512, 1985.

[26] W. Ambrosini, P. Andreussi, and B. J. Azzopardi, “A physically based correlation for drop size in annular flow,” *Int. J. Multiph. Flow*, vol. 17, no. 4, pp. 497–507, Jul. 1991.

[27] T. Fukano, Y. Kawakami, A. Qusaka, and A. Tominaga, “Interfacial shear stress and holdup in an air - water Annular two-phase flow,” in *Proceedings of the ASME-JSME Thermal Engineering Joint Conference: Reno, Nevada, March 17-22, 1991*, 1991, vol. 2, p. 217.

[28] A. J. Holt, B. J. Azzopardi, and M. W. Biddulph, “Calculation of Two-Phase Pressure Drop for Vertical Upflow in Narrow Passages by Means of a Flow Pattern Specific Model,” *Chem. Eng. Res. Des.*, vol. 77, no. 1, pp. 7–15, 1999.

[29] S. Wongwises and W. Kongkiatwanitch, “Interfacial friction factor in vertical upward gas-liquid annular two-phase flow,” *Int. Commun. Heat Mass Transf.*, vol. 28, no. 3, pp. 323–336, 2001.

[30] M. H. S. Zangana, “Film behaviour of vertical gas-Liquid Flow in a large diameter pipe,” no. May, p. 222, 2011.

[31] A. Skopich, E. Pereyra, C. Sarica, and M. Kelkar, “Pipe-diameter effect on liquid loading in vertical gas wells,” *SPE Prod. Oper.*, vol. 30, no. 2, pp. 164–176, 2015.

[32] D. G. Owen, “An experimental and theoretical analysis of equilibrium annular flows,” University of Birmingham, 1986.

[33] C. J. Shearer and R. M. Nedderman, “Pressure gradient and liquid film thickness in co-current upwards flow of gas/liquid mixtures: Application to film-cooler design,” *Chem. Eng. Sci.*, vol. 20, no. 7, pp. 671–683, Jul. 1965.

[34] P. Alia, L. Cravarolo, A. Hassid, and E. Pedrocchi, “Phase and Velocity Distribution in Two-phase Adiabatic Annular Dispersed Flow,” Milan, Italy, 1968.

[35] L. B. Fore and A. E. Dukler, “Droplet deposition and momentum transfer in annular flow,” *AIChE J.*, vol. 41, no. 9, pp. 2040–2046, Sep. 1995.

[36] L. B. Fore and A. E. Dukler, “Droplet deposition and momentum transfer in annular flow,” *AIChE J.*, vol. 41, no. 9, pp. 2040–2046, 1995.

[37] A. A. Almabrok, “Gas-Liquid two-phase flow in up and down vertical pipes,” Cranfield University, 2014.

[38] A. M. Aliyu, “Vertical annular gas-liquid two-phase flow in large diameter pipes,” Cranfield University, 2015.

[39] A. A. Almabrok, A. M. Aliyu, L. Lao, and H. Yeung, “Gas/liquid flow behaviours in a downward section of large diameter vertical serpentine pipes,” *Int. J. Multiph. Flow*, vol. 78, pp. 25–43, 2016.

[40] A. M. Aliyu, L. Lao, A. A. Almabrok, and H. Yeung, “Interfacial shear in adiabatic downward gas/liquid co-current annular flow in pipes,” *Exp. Therm. Fluid Sci.*, vol. 72, pp. 75–87, 2016.

[41] M. W. E. Coney, “The theory and application of conductance probes for the measurement of liquid film thickness in two-phase flow,” *J. Phys. E.*, vol. 6, no. 9, pp. 903–911, Sep. 1973.

[42] J. E. Koskie, I. Mudawar, and W. G. Tiederman, “Parallel-wire probes for measurement of thick liquid films,” *Int. J. Multiph. Flow*, vol. 15, no. 4, pp. 521–530, 1989.

[43] N. A. Tsochatzidis, T. D. Karapantsios, M. V. Kostoglou, and A. J. Karabelas, “A conductance probe for measuring liquid fraction in pipes and packed beds,” *Int. J. Multiph. Flow*, vol. 18, no. 5, pp. 653–667, 1992.

[44] B.-A. Lee, B.-J. Yun, K.-Y. Kim, and S. Kim, “Estimation of local liquid film thickness in two-phase annular flow,” *Nucl. Eng. Technol.*, vol. 44, no. 1, pp. 71–78, Feb. 2012.

[45] H.-M. Prasser, M. Beyer, H. Carl, S. Gregor, D. Lucas, H. Pietruske, P. Schütz, and F.-P. Weiss, “Evolution of the structure of a gas–liquid two-phase flow in a large vertical pipe,” *Nucl. Eng. Des.*, vol. 237, no. 15–17, pp. 1848–1861, Sep. 2007.

[46] M. J. Da Silva, S. Thiele, L. Abdulkareem, B. J. Azzopardi, and U. Hampel, "High-resolution gas–oil two-phase flow visualization with a capacitance wire-mesh sensor," *Flow Meas. Instrum.*, vol. 21, no. 3, pp. 191–197, Sep. 2010.

[47] M. J. Da Silva, E. Schleicher, and U. Hampel, "Capacitance wire-mesh sensor for fast measurement of phase fraction distributions," *Meas. Sci. Technol. Meas. Sci. Technol*, vol. 18, no. 18, pp. 2245–2251, 2007.

[48] M. J. Da Silva, S. Thiele, L. Abdulkareem, B. J. Azzopardi, and U. Hampel, "High-resolution gas – oil two-phase flow visualization with a capacitance wire-mesh sensor," *Flow Meas. Instrum.*, vol. 21, no. 3, pp. 191–197, 2010.

[49] N. Hall Taylor, G. F. Hewitt, and P. M. C. Lacey, "The motion and frequency of large disturbance waves in annular two-phase flow of air-water mixtures," *Chem. Eng. Sci.*, vol. 18, pp. 537–552, 1963.

[50] P. Sawant, M. Ishii, T. Hazuku, T. Takamasa, and M. Mori, "Properties of disturbance waves in vertical annular two-phase flow," *Nucl. Eng. Des.*, vol. 238, no. 12, pp. 3528–3541, 2008.

[51] G. F. Hewitt and N. Hall Taylor, *Annular Two-phase Flow*. Oxford: Pergamon Press, 1970.

[52] K. W. McQuillan and P. B. Whalley, "Flow patterns in vertical two-phase flow," *Int. J. Multiph. Flow*, vol. 11, no. 2, pp. 161–175, 1985.

[53] G. F. Hewitt, "Co-Current and Counter-Current Two Phase Annular Flow," *9th Australasian Fluid Mechanics COnference*. pp. 19–28, 1986.

[54] Q. Al-Yarubi, "Phase flow measurements of annular flows," University of Huddersfield, 2010.

[55] R. E. Vieira, M. Parsi, C. F. Torres, B. S. McLaury, S. A. Shirazi, E. Schleicher, and U. Hampel, "Experimental characterization of vertical gas-liquid pipe flow for annular and liquid loading conditions using dual Wire-Mesh Sensor," *Exp. Therm. Fluid Sci.*, vol. 64, pp. 81–93, 2015.

[56] A. Cioncolini and J. R. Thome, "Entrained liquid fraction prediction in adiabatic and evaporating annular two-phase flow," *Nucl. Eng. Des.*, vol. 243, pp. 200–213, 2012.

[57] M. Ishii and K. Mishima, "Droplet entrainment correlation in annular two-phase flow," *Int J Heat Mass Transf.*, vol. 32, no. 10, pp. 1835–1846, Oct. 1989.

[58] P. Sawant, M. Ishii, and M. Mori, "Prediction of amount of entrained droplets in vertical annular two-phase flow," *Int. J. Heat Fluid Flow*, vol. 30, no. 4, pp. 715–728, 2009.

[59] Y. Taitel, D. Bornea, and A. E. Dukler, “Modelling flow pattern transitions for steady upward gas-liquid flow in vertical tubes,” *AIChE J.*, vol. 26, no. 3, pp. 345–354, May 1980.

[60] G. F. Hewitt and D. N. Roberts, “Studies of Two Phase Patterns by Simultaneous X-Ray and Flash Photography,” Harwell, Berkshire, 1969.

[61] C. J. Shearer and R. M. Nedderman, “Pressure gradient and liquid film thickness in concurrent upwards flow of gas/liquid mixtures: application to film cooler design,” *Chem. Eng. Sci.*, vol. 20, no. 671, pp. 671–683, 1965.

[62] Shell, “Gas / Liquid Separators - Type Selection and Design Rules Manual,” 2007.

[63] B. J. Azzopardi, “Mechanisms of entrainment in annular two phase flow.PDF,” Harwel, Oxfordshire, UK, 1983.

[64] S. Jayanti, A. Tokarz, and G. F. Hewitt, “Theoretical investigation of the diameter effect on flooding in countercurrent flow,” *Int. J. Multiph. Flow*, vol. 22, no. 2, pp. 307–324, Apr. 1996.

[65] G. B. Wallis, “The onset of droplet entrainment in annular gas-liquid flow,” General Electric Co. General Engineering Lab., Schenectady, NY, RPRT, 1962.

[66] J. R. Barbosa, G. F. Hewitt, G. König, and S. M. Richardson, “Liquid entrainment, droplet concentration and pressure gradient at the onset of annular flow in a vertical pipe,” *Int. J. Multiph. Flow*, vol. 28, no. 6, pp. 943–961, 2002.

[67] A. Cioncolini, J. R. Thome, and C. Lombardi, “Algebraic turbulence modeling in adiabatic gas-liquid annular two-phase flow,” *Int. J. Multiph. Flow*, vol. 35, no. 6, pp. 580–596, 2009.

[68] M. Narcy, “flow boiling in straight heated tube under normal and microgravity conditions,” University of Toulouse, 2015.

Figures:

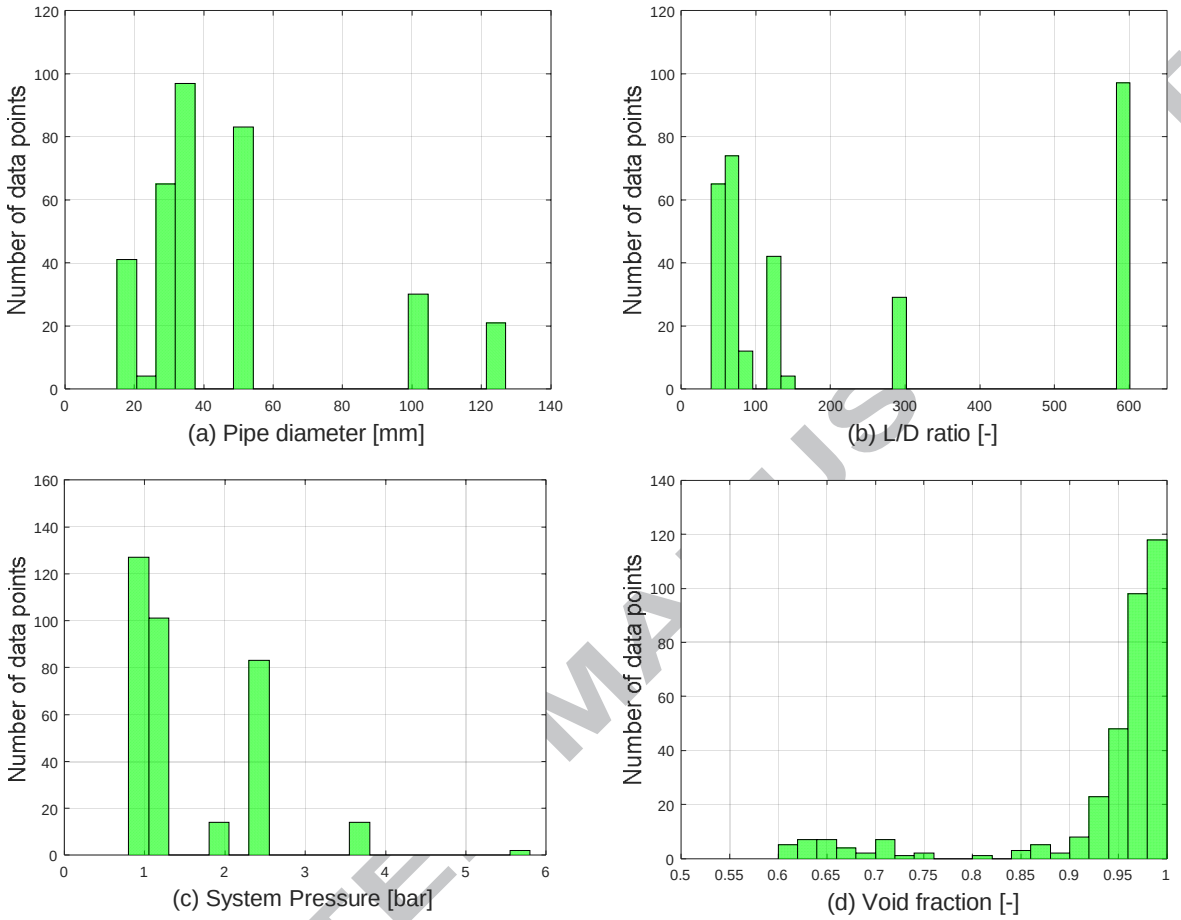

Figure 1: Histograms showing selected parameters of the experimental database given in Error! Reference source not found.

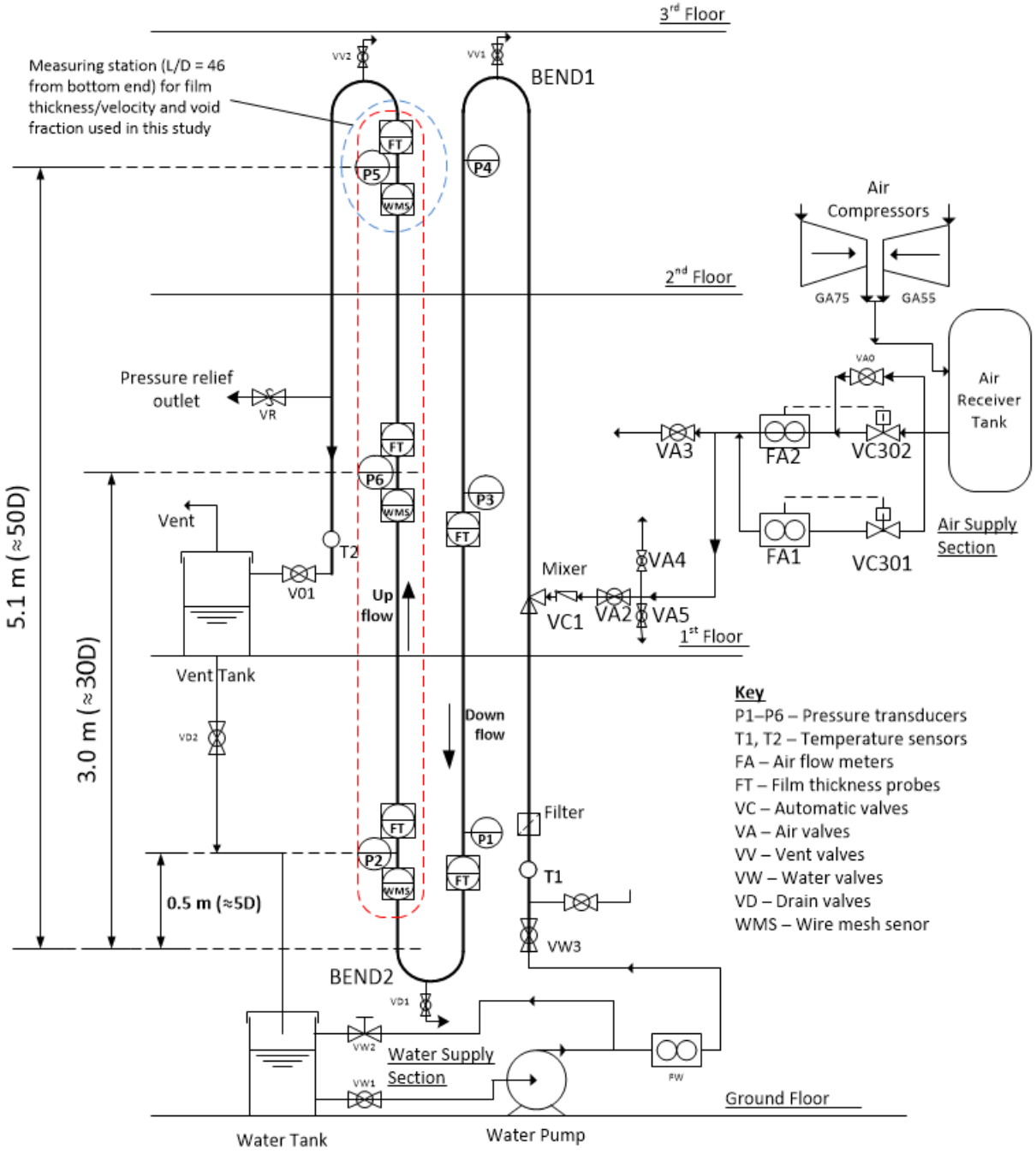

Figure 2: Serpent Rig facility indicating the upward section used for this study

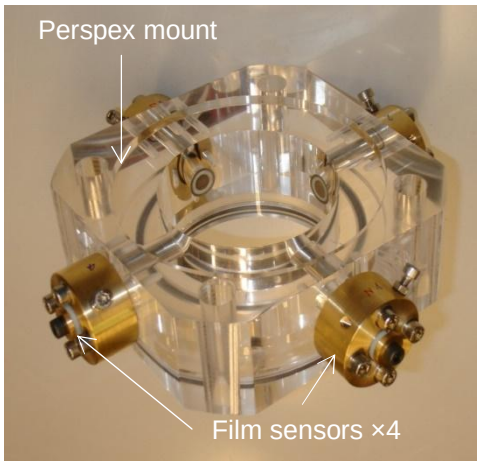

(a)

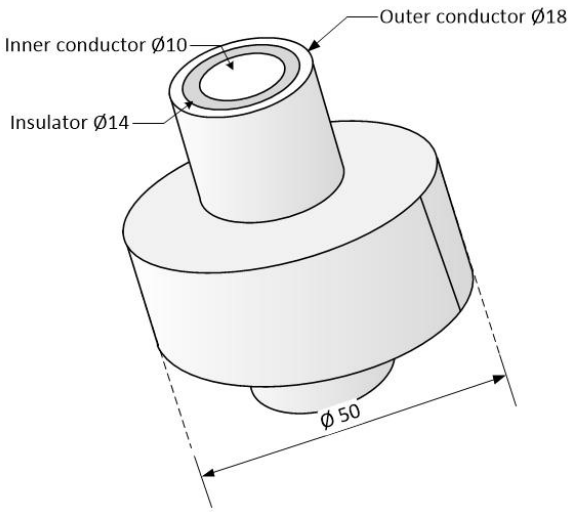

(b)

(c)

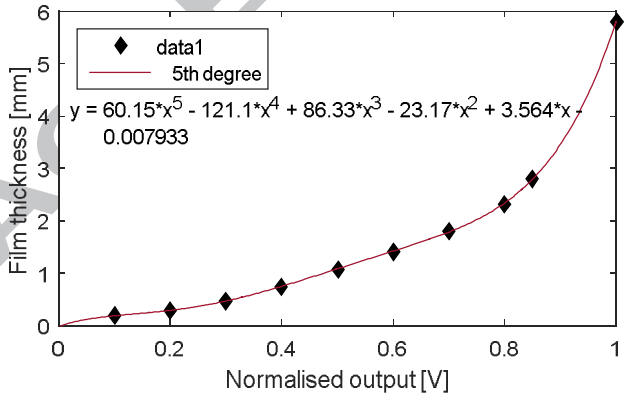

(d)

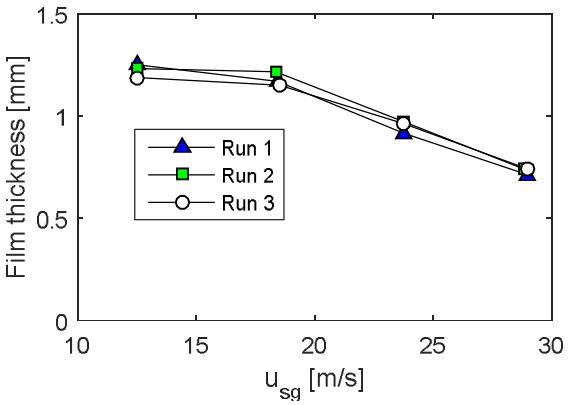

(e)

Figure 3: (a) film thickness sensor spool with four flush-mounted probes (b) details of individual sensor design (all dimensions in mm) (c)) blocks of different diameters used for probe calibration (d) sample of film thickness calibration curve (e) Repeatability tests for film thickness probes showing the mean film thickness at u_{sl} = 0.1 m/s. For more conditions, see Almabrok [37]

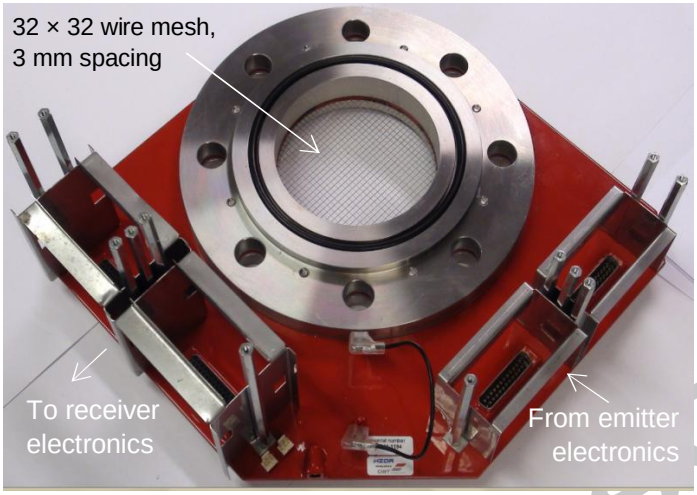

Figure 4: Capacitance wire mesh sensor used in this study

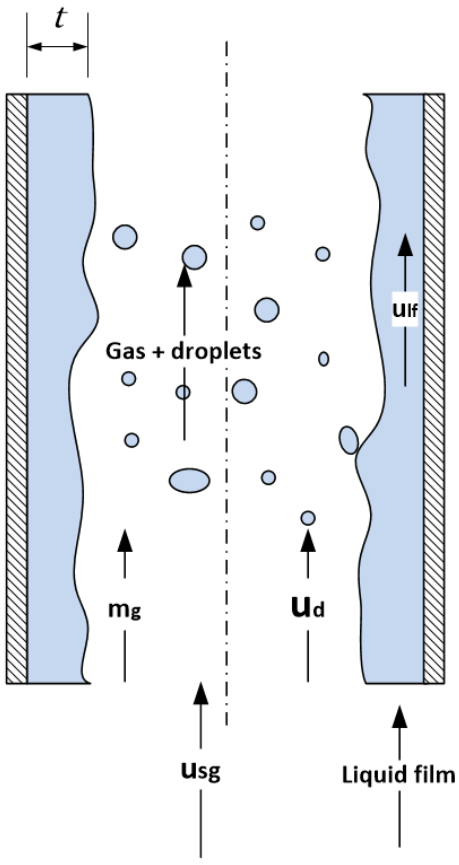

Figure 5: Representation of annular flow with droplets

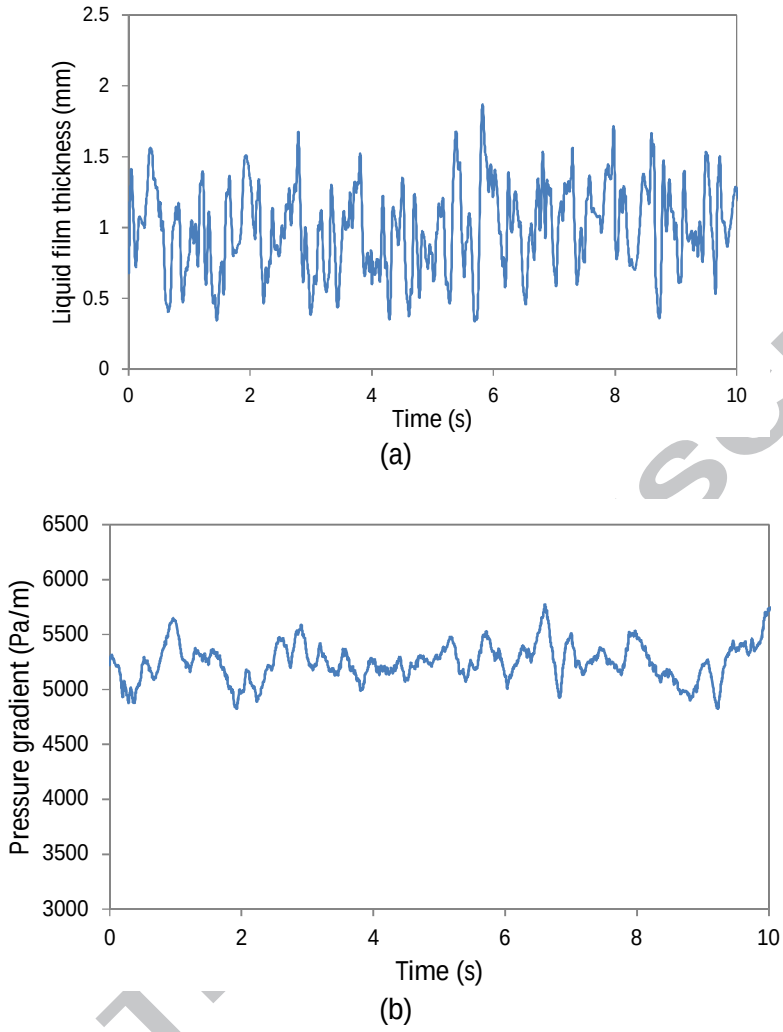

Figure 6: Examples of time series data for (a) liquid film thickness and (b) pressure gradient with a superficial liquid velocity of 1.0 m/s and superficial gas velocity of 18.56 m/s

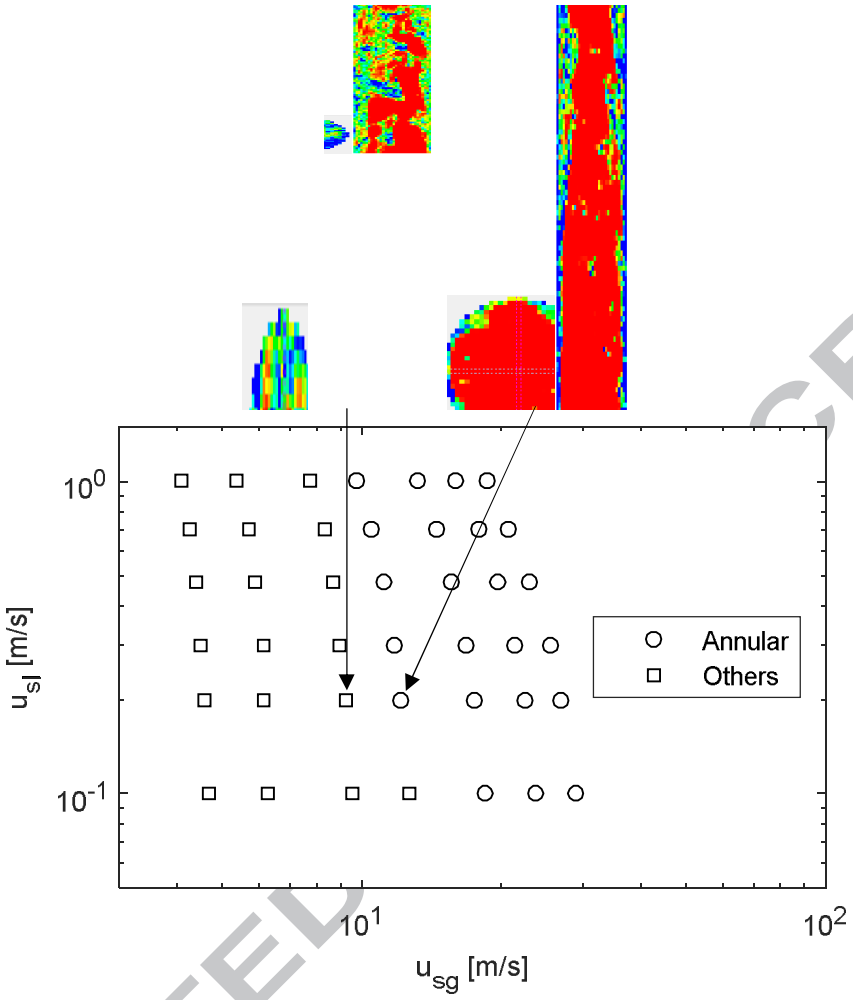

Figure 7: Effect of fluid superficial velocities on flow regime map produced by visual observations aided by WMS visualisation

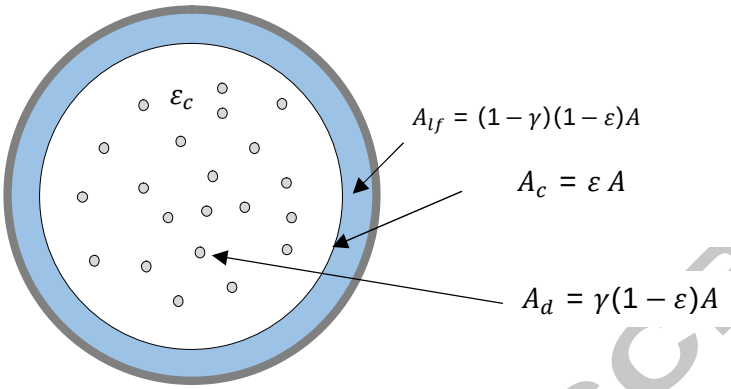

Figure 8: Representation and notation of the various phases (film, gas, and droplets) occupying the total pipe area. Subscript *d* denotes droplets. Where γ, ε, and ε_c are the droplet holdup, void fraction and core void fraction respectively (Cioncolini et al. [22]**)**

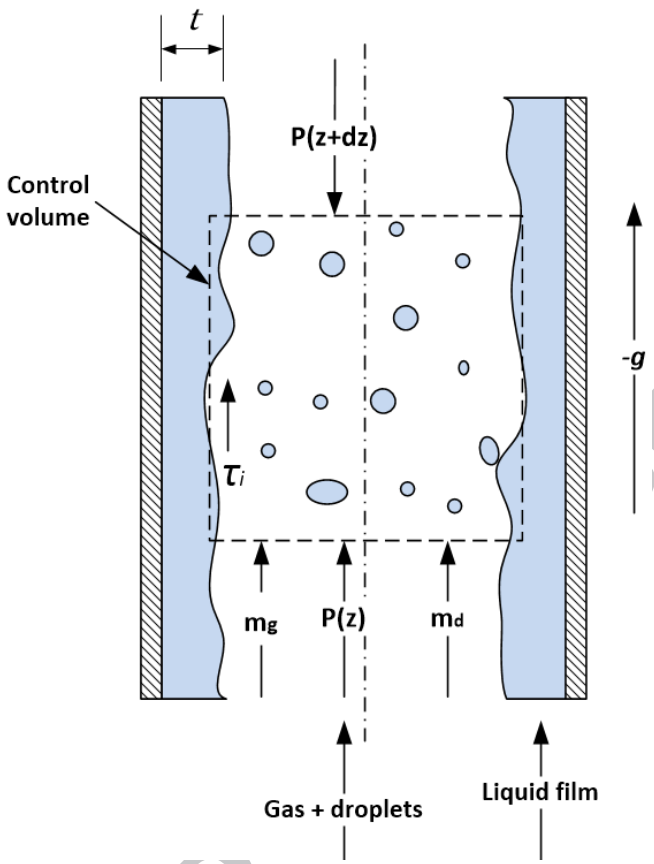

Figure 9: Control volume for the momentum balance in Equation Error! Reference source not found.**.**
Based on the schematic by Wongwises and Kongkiatwanitch [29]

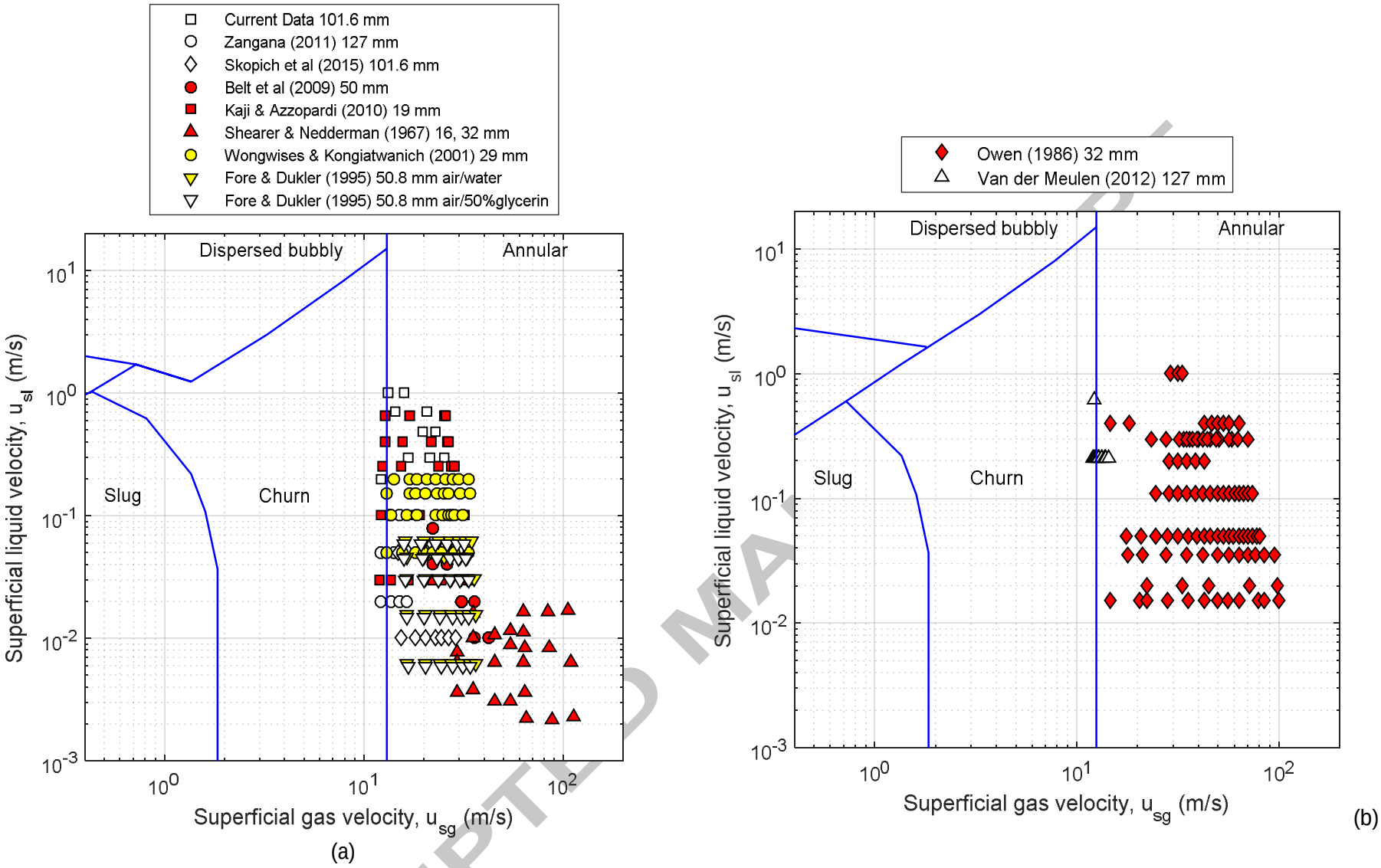

Figure 10: Experimental data against the Taitel et al. [59] **flow regime map**

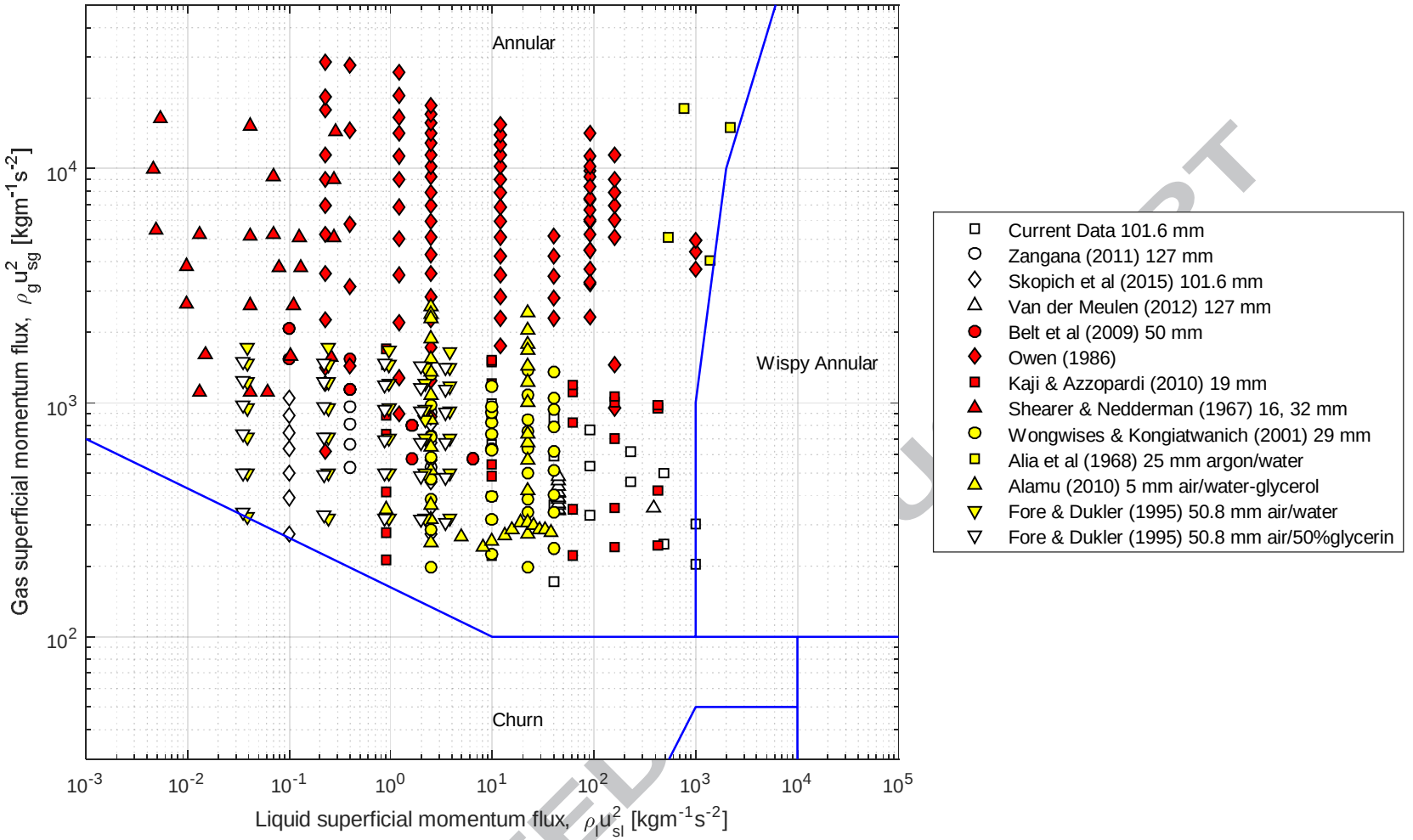

Figure 11: Experimental data bank against Hewitt and Roberts [60] **flow regime map showing all data are in the annular flow regime**

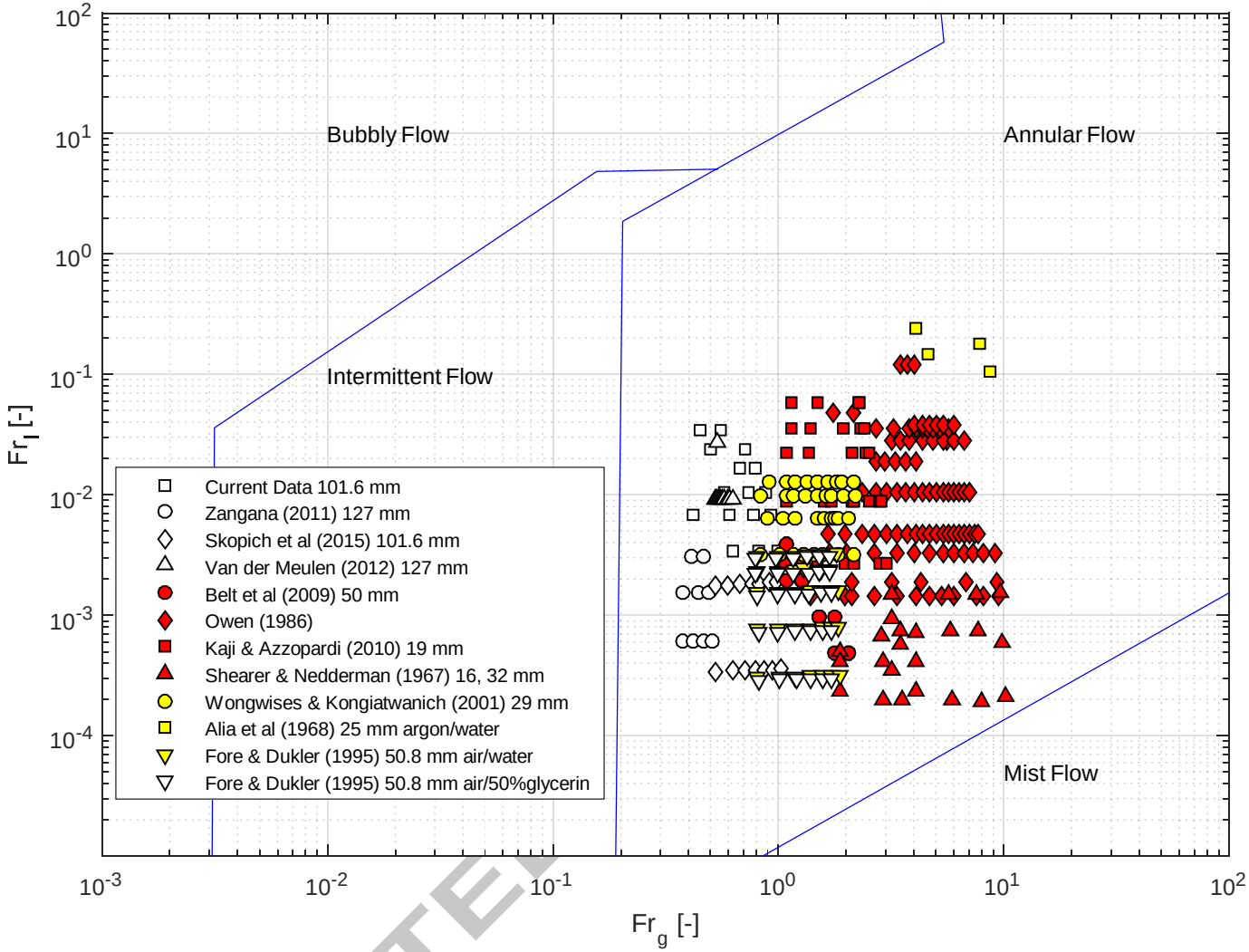

Figure 12: experimental databank against the Shell [62] **flow regime map**

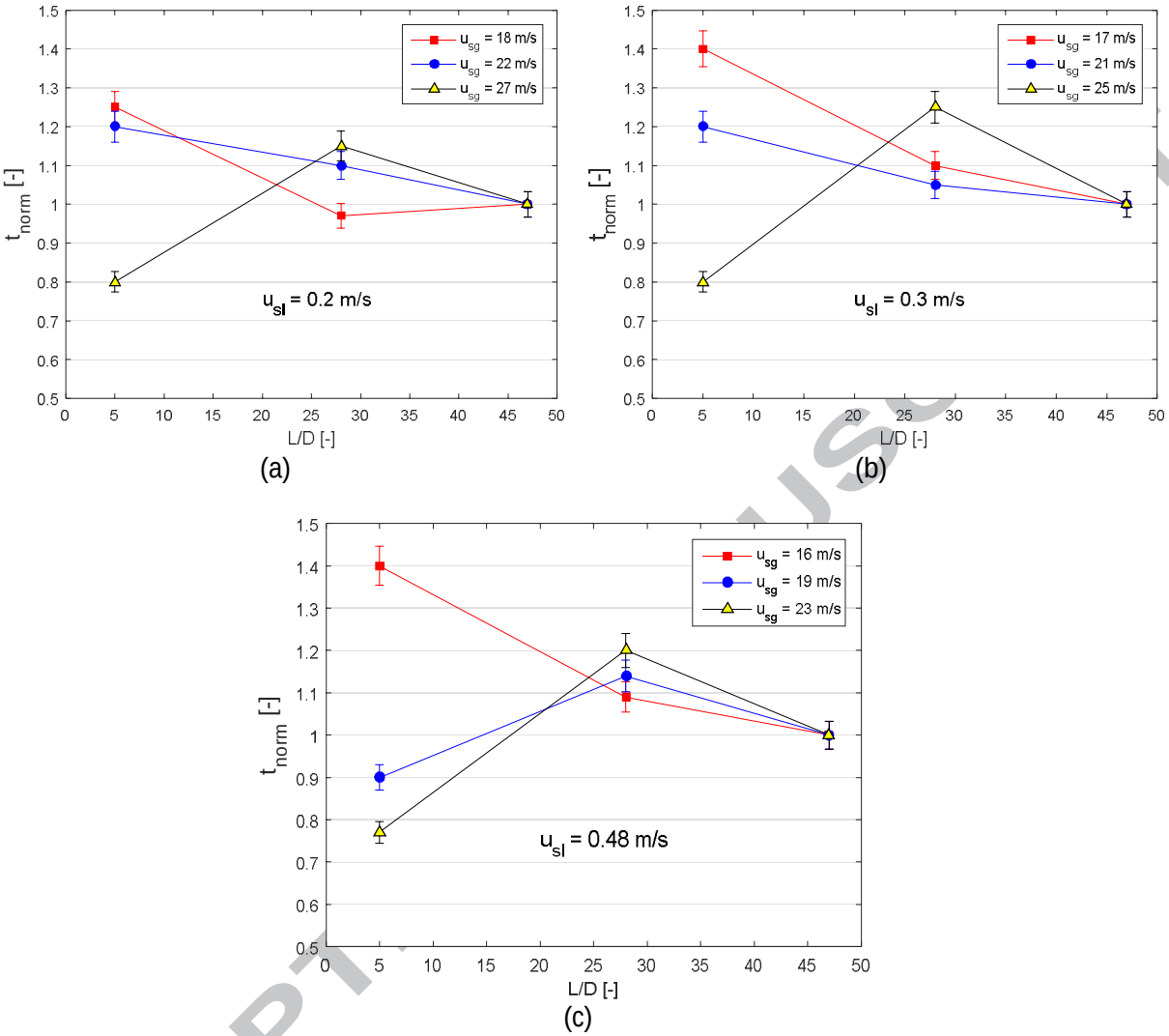

Figure 13: Normalised liquid film thickness axial development in the upwards flowing section of the rig (See Almabrok [37] for more)

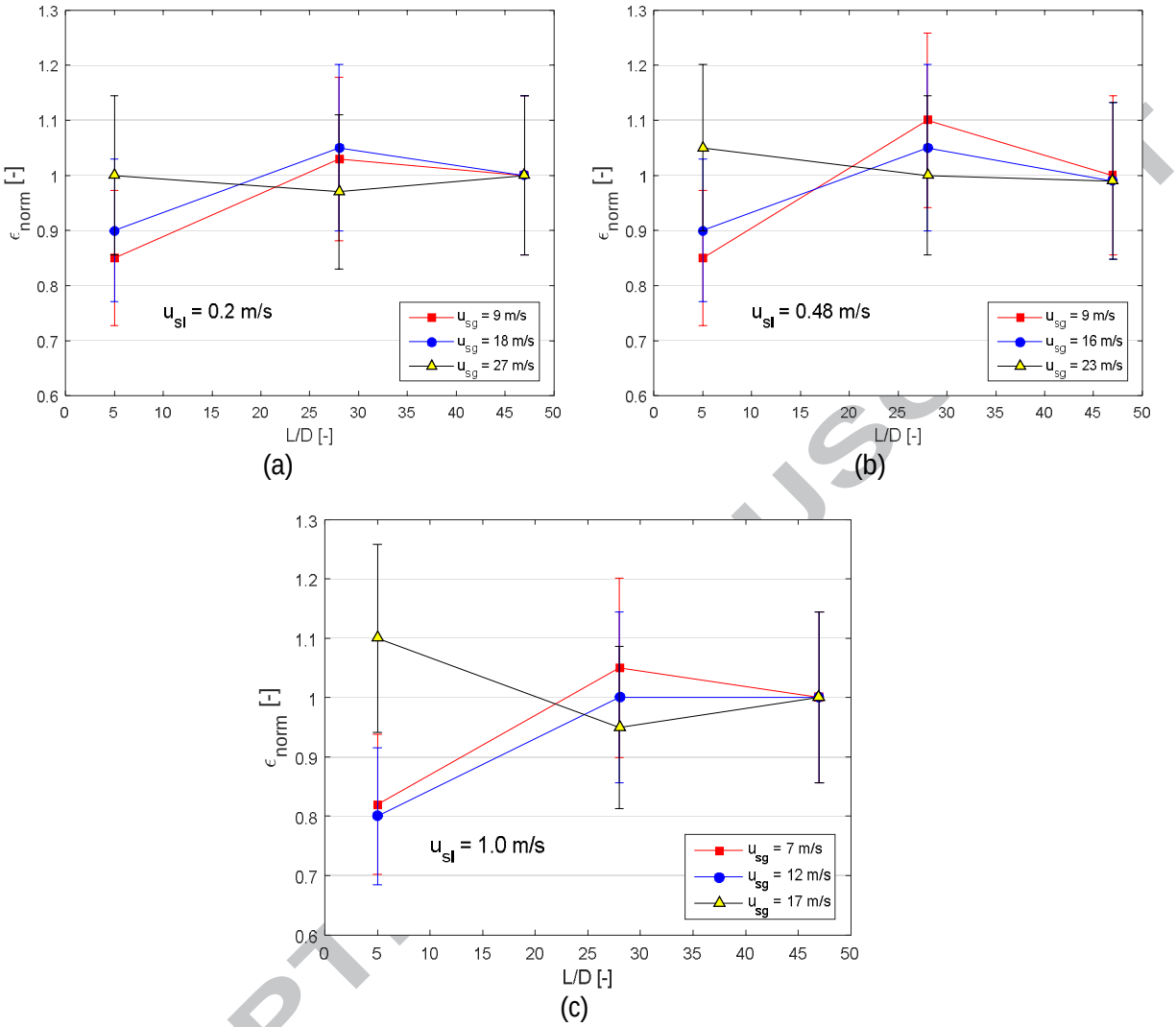

Figure 14: Normalised gas void fraction axial development in the upwards flowing section of the rig

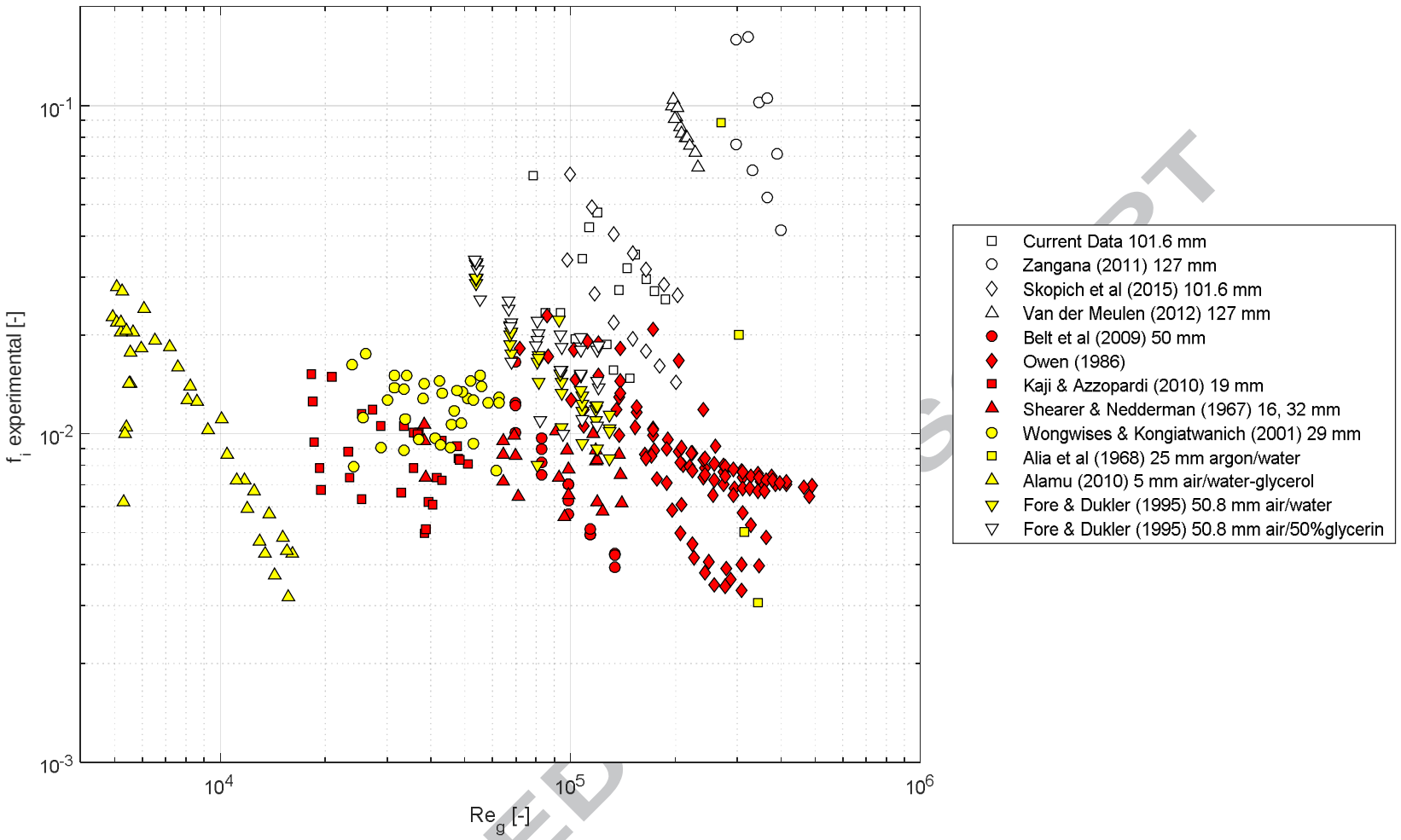

Figure 15: Experimental interfacial friction factors versus superficial gas Reynolds number

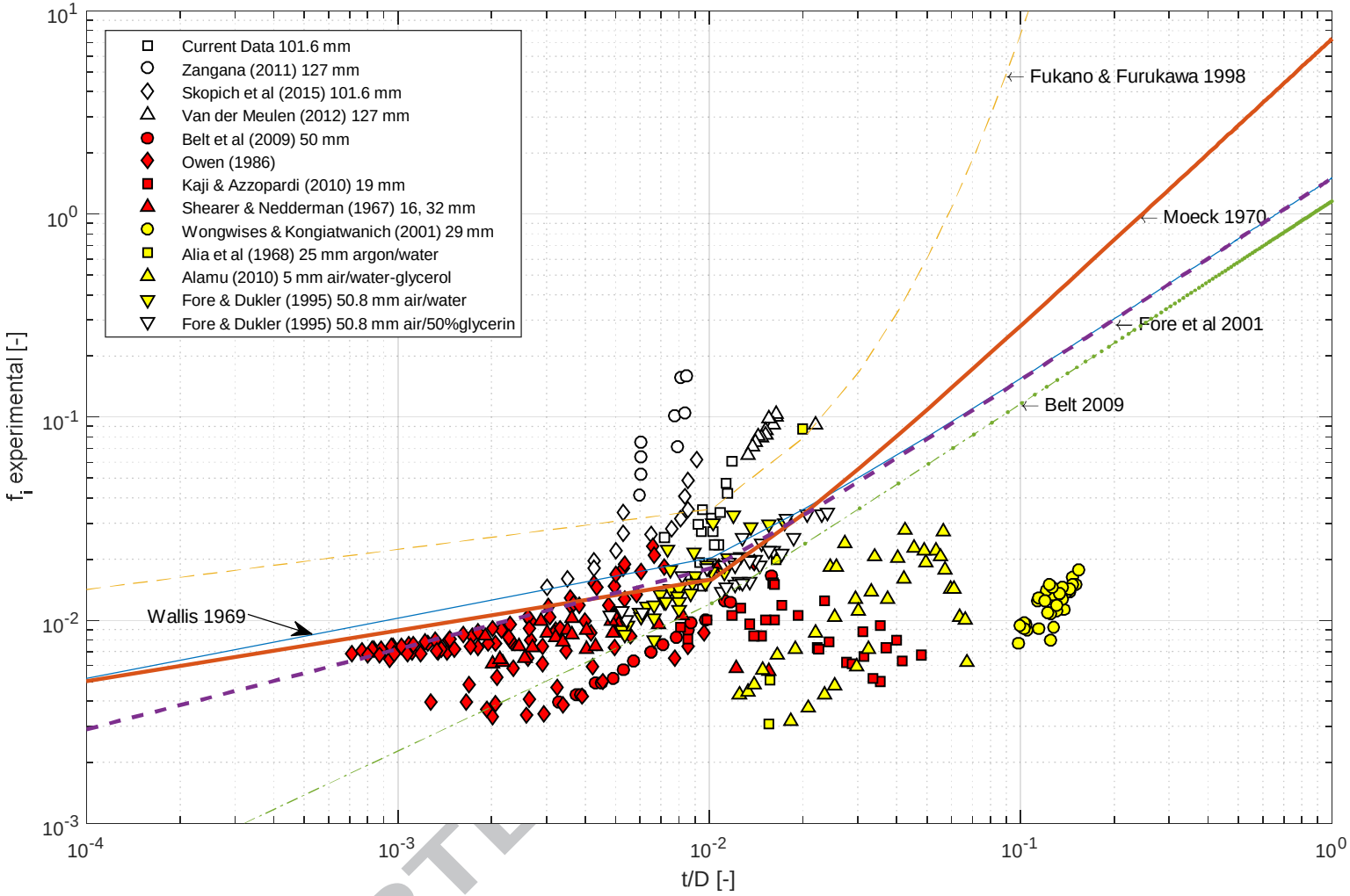

Figure 16: Comparison of current and other experimental friction factors with Wallis-type correlations

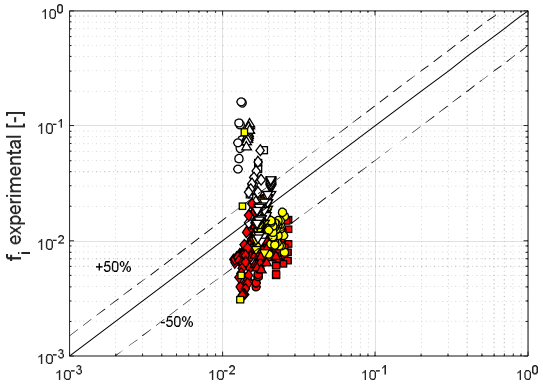

(a) f_i calculated (Blasius 1913) [-]

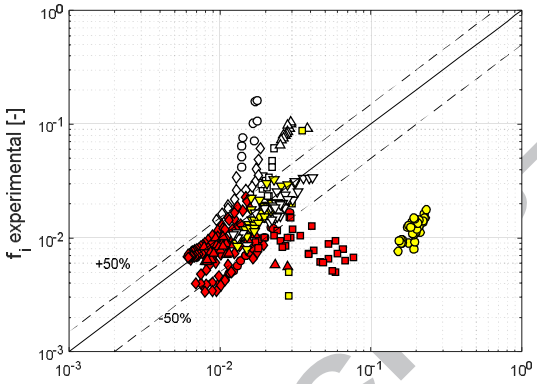

(b) f_i calculated (Wallis 1969) [-]

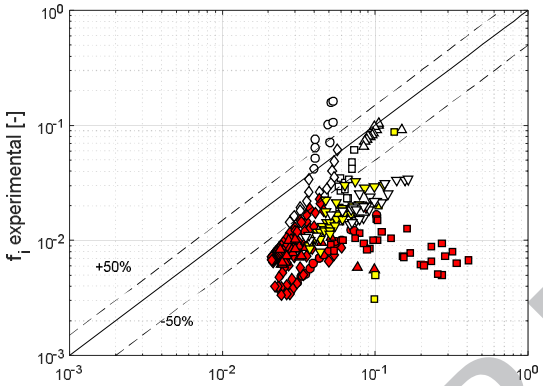

(c) f_i calculated (Moeck 1970) [-]

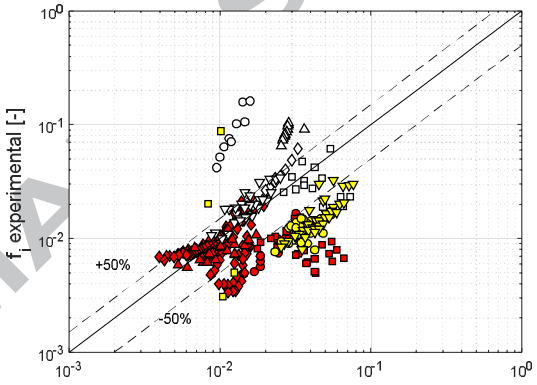

(d) f_i calculated (Hori 1976) [-]

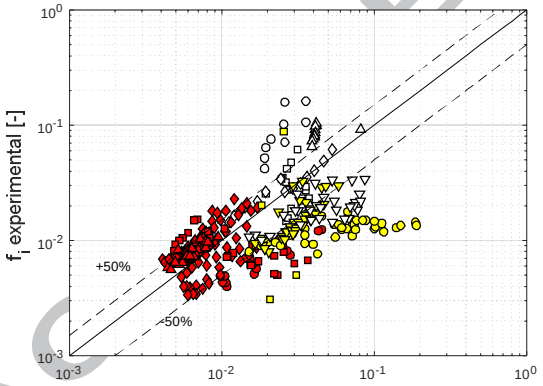

(e) f_i calculated (Asali et al 1985) [-]

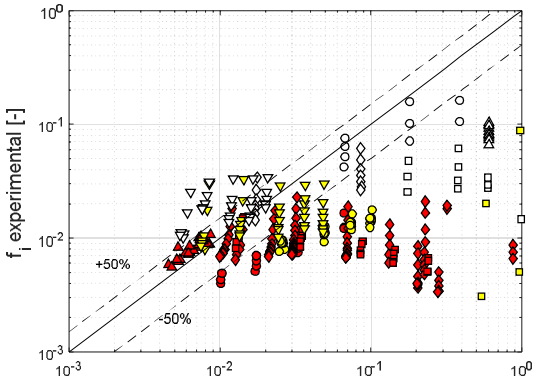

(f) f_i calculated (Fukano et al 1985) [-]

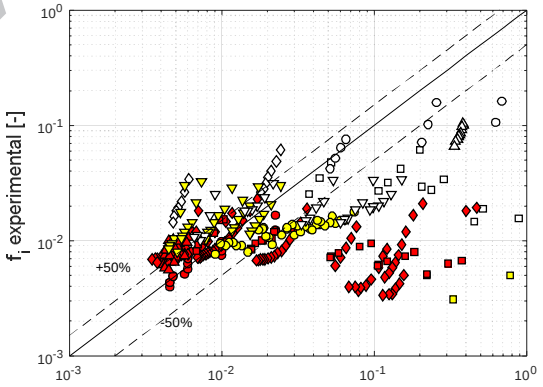

(g) f_i calculated (Fukano et al 1991) [-]

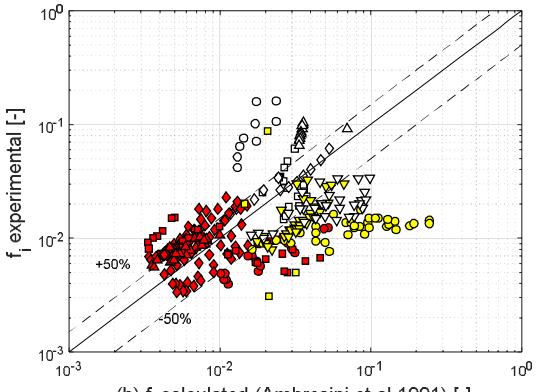

(h) f_i calculated (Ambrosini et al 1991) [-]

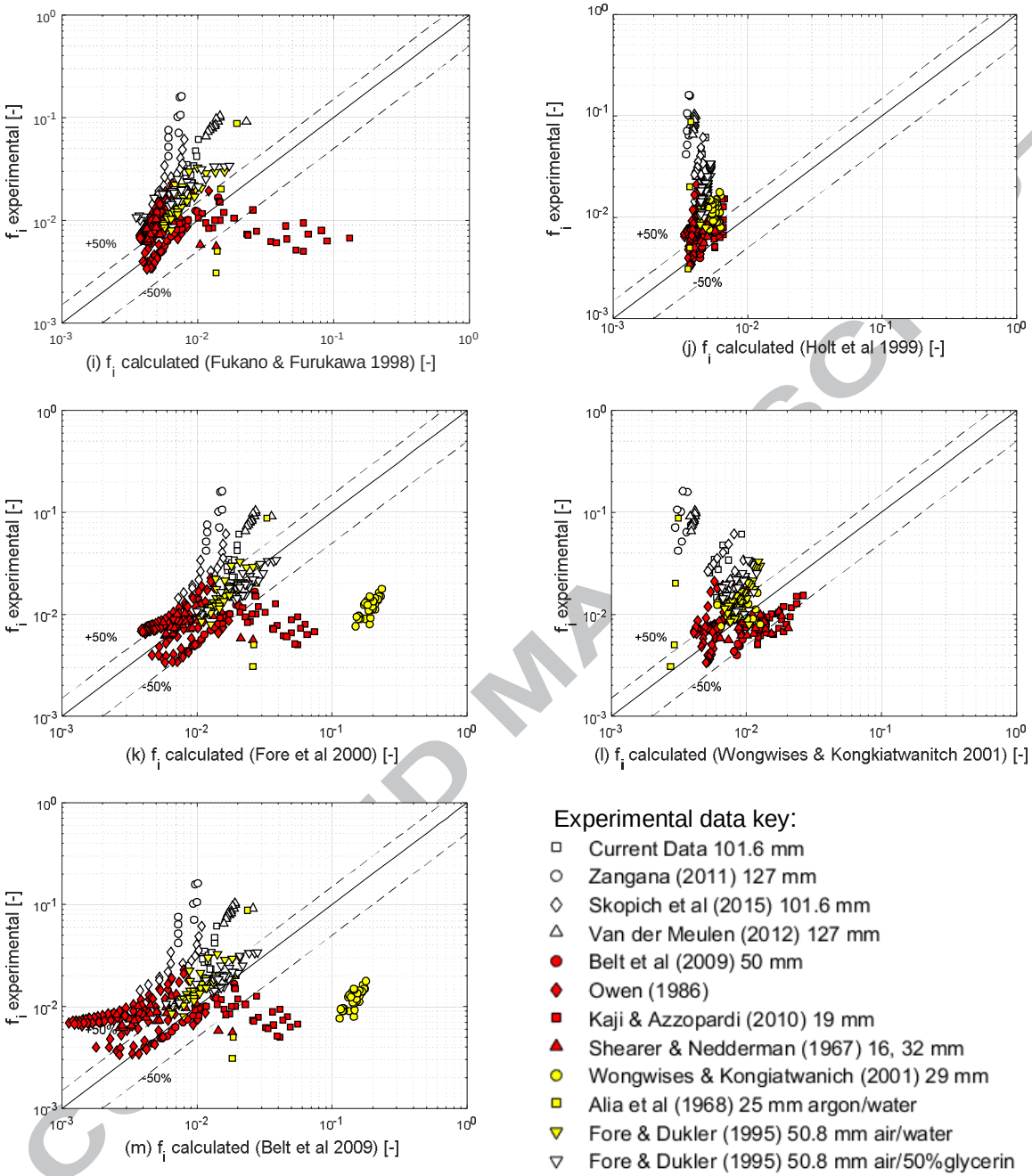

Figure 17: Comparison of 332 interfacial friction factor data points with predictions of various correlations

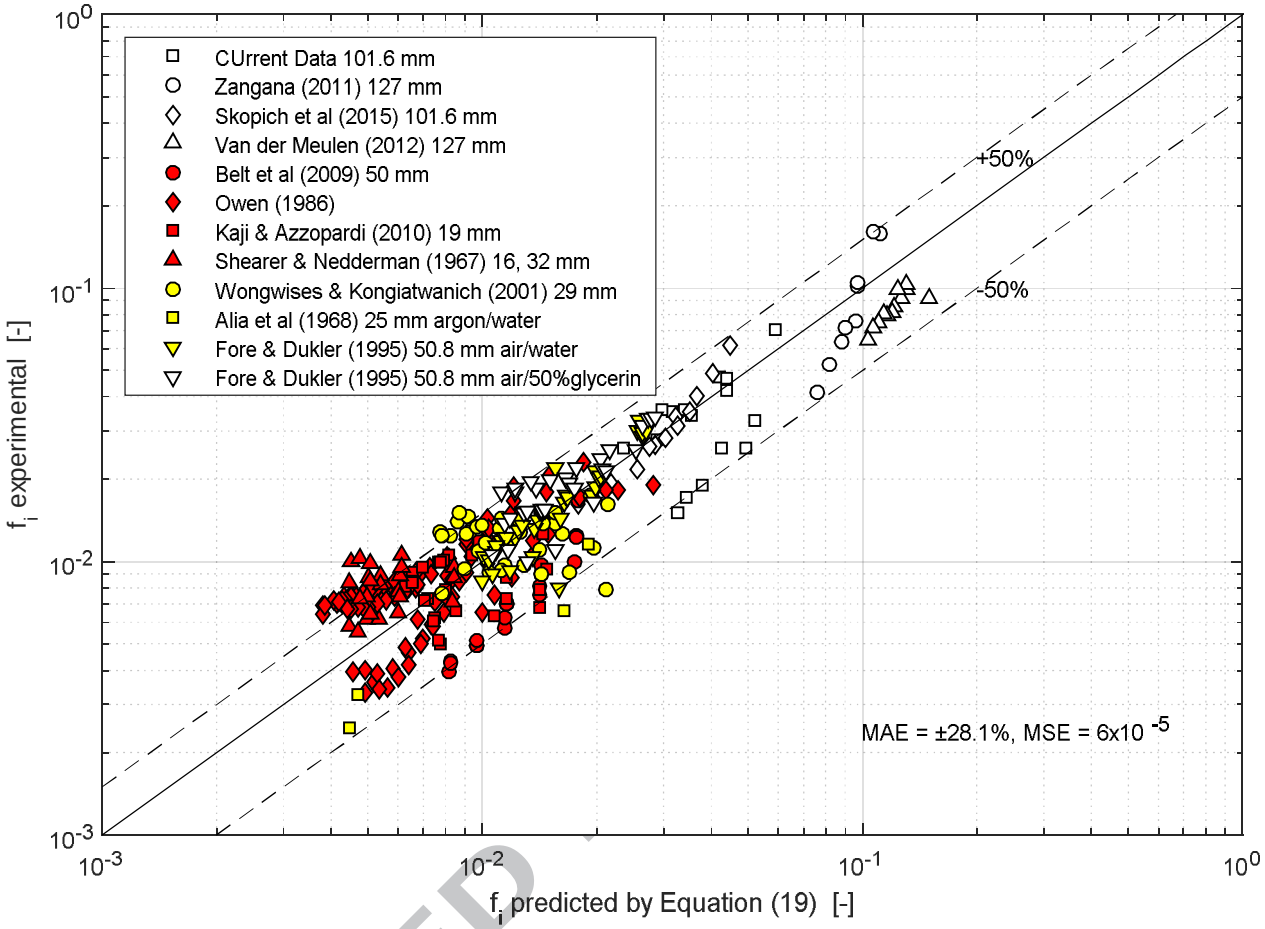

Figure 18: Predictions of proposed correlation compared with entire experimental database

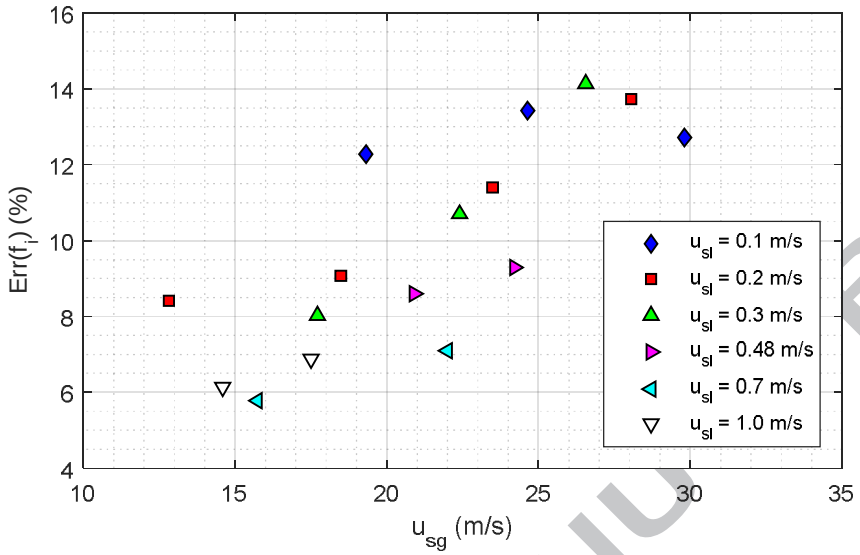

Figure A1: Experimental uncertainties in f_i

Tables

Table 1: Reported interfacial friction factor correlations used for comparison with the current experimental data

Author(s)	Equation	Remarks
Blasius	$f_i = 0.316\,Re_g^{-0.25}$	Valid for Re up to 10^5
Wallis [2]	$f_i = 0.005[1 + 300t/D]$	Theoretical model
Moeck [3]	$f_i = 0.005[1 + 1458(t/D)^{1.42}]$	Pipe 24 mm, steam/water
Hori et al. [24]	$f_i = 1.13\,Re_g^{-0.89}Re_l^{0.68}Fr_g^{0.25}Fr_l^{-0.45}(\mu_l/\mu_w)^{0.7}$, $Fr_g = u_{sg}/\sqrt{gD}$, $Re_g = \rho_g u_{sg} D/\mu_g$	Pipe 13, 19.8, 26 mm, u_{sg} = 53–56 m/s, u_{sl} = 0.006–0.0061 m/s
Asali et al. [5]	$f_i = f_g\left[1 + Re_g^{-0.2}\left(Re_g\sqrt{f_i/2}\ t/D - 4\right)\right]$, where $f_g = 0.316\,Re_g^{-0.25}$	Pipe 22.9, 42 mm, air/water, air/glycerine, 1–2 bar system pressure
Fukano et al. [25]	$f_i = f_g\left[1 + 1\times10^{-5}Re_g^{0.7}Re_l^{0.65}X^{0.52}\right]$, $X = \sqrt{\frac{\Delta P_{lo}}{\Delta L}/\frac{\Delta P_{go}}{\Delta L}}$, $\Delta P_{LO}/\Delta L = \frac{1}{2}(f_L/D)\rho_L u_{sl}^2$, $\Delta P_{gO}/\Delta L = \frac{1}{2}(f_g/D)\rho_g u_{sg}^2$	Rectangular duct, 80×10 mm, air/water, 0.98–1 bar pressure, Re_l = 10–300, u_{sg} = 10–50 m/s
Ambrosini et al. [26]	$f_i = f_g\left[1 + 13.8We^{0.2}Re_g^{-0.6}\left(t^+ - 200\sqrt{\rho_g/\rho_l}\right)\right]$, for $\dot{m} > 100\ kgm^{-2}s^{-1}, where\ t_g^+ = 0.19Re_{lf}^{0.7}$	Pipe 10–42.2 mm, air/water, helium/water, air/various hydrocarbons, 0.2 – 1.9 bar
Fukano et al. [27]	$f_i = f_g\left[1 + 8.53\times10^{-4}\,X^{2.82}Re_g^2/Re_l\right]$	Pipe, 10, 16, 26 mm, 1.02 – 1.35 bar, u_{sg} = 20 – 60 m/s, u_{sl} = 0.06 – 0.1 m/s
Fukano and Furukawa [23]	$f_i = 0.425(12 + v_l/v_w)^{-1.33}(1 + 12t/D)^8$	Pipe 4.6 mm, air/water, air/glycerol, 1–1.2 bar, u_{sg} = 10–50 m/s, u_{sl} = 0.04–0.3 m/s
Holt et al. [28]	$f_i = f_g\left[1 + 13.8We^{0.175}Re_g^{-0.7}\right]$, for $\dot{m} > 100\ kgm^{-2}s^{-1}$	Pipe 5, 10 mm, square duct 7.7×2.6 mm, trapezoidal duct, 2×7×4.4 mm, air/water, nitrogen/water, helium/water, air/glycerol, 0.2–1.5 bar pressure
Fore et al. [6]	$f_i = 0.005[1 + 300(t/D - 0.0015)]$	Rectangular duct, 101.6×5.08 mm, nitrogen/water, 3.4–17 bar
Wongwises and Kongkiatwanitch [29]	$f_i = 17.172\,Re_g^{-0.768}(t/D)^{-0.253}$	Pipe 29 mm, air/water, 1 bar pressure
Belt et al. [1]	$f_i = 1.158t/D + 3.143\times10^{-4}$	Pipe 19 mm, air/water, 1 bar pressure

Table 2: Experimental data for upward interfacial friction factor (all air/water except stated otherwise)

S/No.	Authors	D [mm]	L/D [-]	Test pressure [bara]	u_{sl} range [m/s]	u_{sg} range [m/s]	Measurements made	Number of data points	Symbol
1	Current	101.6	46	1.0–1.4	0.1-1.0	10–29	dP/dz, t, u_{lf}	23	
2	Zangana [30]	127	66	1.0	0.02–1.00	10–17	dP/dz, ε, τ_w	9	
3	Skopich et al. [31]	101.6	58 – 92	0.9–1.2	0.01–0.05	14–27	dP/dz, ε	14	
4	Van der Meulen [17]	127	87	2.0	0.02–0.70	10–17	dP/dz, ε	12	
5	Belt et al. [1]	50	120, 140	1.0	0.01–0.08	22–42	dP/dz, t	18	
6	Owen [32]	32	600	2.0–4.0	0.02–1.00	14–100	dP/dz, *e*	97	
7	Kaji and Azzopardi [11]	19	300	1.2	0.03–0.65	10–34	dP/dz, ε	29	
8	Shearer and Nedderman [33]	16, 32	133–267	1.1	0.02–0.10	10–16	dP/dz, t	24	
9	Wongwises and Kongkiatwanitch [29]	29	41	1.0	0.05–0.2	9–34	dP/dz, t	35	
10	Alia et al. [34]*	25	140	2–6	0.07–1.5	7–150	dP/dz, t	6	
11	Fore and Dukler [35]	50.8	69	1.0	0.006–0.06	16–36	dP/dz, t, e, τ_w	35	
12	Fore and Dukler [35]**	50.8	69	1.0	0.006–0.06	16–36	dP/dz, t, e, τ_w	30	
	Total							332	

*Argon–Water, ** Air–50%glycerin, fluid combination

Table 3: Averaged measured quantities for the air–water system in the upward section of the Serpent Rig

Test Pressure (bara)	u_{sl} (m/s)	u_{sg} (m/s)	t (mm)	u_{lf} (m/s)	dP/dz (Pa/m)
1.09	0.10	18.39	1.2	0.86	1039.2
1.13	0.10	23.66	1.0	1.00	1268.6
1.15	0.10	28.87	0.7	1.01	1592.2
1.10	0.20	12.08	1.2	0.78	1680.4
1.14	0.20	17.51	1.2	0.80	1419.6
1.18	0.20	22.41	1.0	1.02	1488.2
1.23	0.20	26.90	1.0	2.02	1576.5
1.13	0.30	11.70	1.3	0.74	1878.4
1.18	0.30	16.74	1.1	0.73	2505.9
1.23	0.30	21.33	1.0	1.03	2172.5
1.29	0.30	25.47	0.9	2.03	1890.2
1.17	0.48	11.16	1.2	0.98	1794.1
1.25	0.48	15.63	1.1	1.08	1839.2
1.32	0.48	19.62	1.0	1.10	2045.1
1.40	0.48	22.87	1.0	1.14	2441.2
1.23	0.70	10.50	1.1	0.89	3068.6
1.33	0.70	14.45	1.1	1.10	2452.9
1.42	0.70	17.91	1.0	1.12	2149.0
1.53	0.70	20.59	0.9	1.19	2145.1
1.32	1.00	9.65	1.2	0.94	2284.3
1.44	1.00	13.15	1.1	1.30	2772.5
1.56	1.00	15.98	1.0	1.37	3260.8
1.67	1.00	18.56	0.9	1.42	3937.3

Table 4: Statistical comparison between predictions of proposed and previous correlations

Correlation \ Statistic	MSE*	MAE**	Percentage of points within ±50% error band
Proposed	0.00006	28.1	83.85
Blasius	0.00051	123.3	28.57
Wallis [2]	0.00412	259.7	49.69
Moeck [3]	0.27280	1814.1	6.83
Hori et al. [24]	0.00067	139.5	43.48
Asali et al. [5]	0.00099	115.2	49.38
Ambrosini et al. [26]	0.00157	143.0	44.72
Fukano et al. [27]	0.06933	678.6	46.89
Fukano & Furukawa [23]	5.59788	5468.3	45.03
Holt et al. [28]	0.00066	139.5	36.34
Fore et al. [6]	0.00404	231.6	57.76
Wongwises & Kongkiatwanich [29]	0.00062	49.6	54.97
Belt et al. [1]	0.00250	185.3	41.93

*MSE is the Mean Square Error defined as $\frac{1}{n}\sum_i^n \left(f_{i,exp} - f_{i,pred}\right)^2$

**MAE is the percentage Mean Absolute Error defined as $\frac{1}{n}\sum_i^n \left|\frac{f_{i,exp}-f_{i,pred}}{f_{i,exp}}\right| \times 100$

Highlights

- Gas–liquid two-phase flow experiments conducted in a large diameter flow loop
- Data were collected for interfacial friction factor in upwards annular flow regimes
- Data were also gathered from other sources spanning both small and large diameter pipes
- Previous correlations' predictions deviated at high shear regions mainly for large pipes
- Improved correlation is proposed to fit the diverse database of more than 300 data points